1 **Adaptive robustness through incoherent signaling mechanisms in a regenerative brain**

2

3 Samuel R. Bray[1‡], Livia S. Wyss[2‡], Chew Chai[1], Maria E. Lozada[1,3], Bo Wang[1]*

4

5 [1]Department of Bioengineering, Stanford University, Stanford, CA, USA

6 [2]Department of Biology, Stanford University, Stanford, CA, USA

7 [3]Department of Biomedical Engineering, University of Miami, Coral Gables, FL, USA

8

9 [‡] these authors contributed equally to this work

10 *correspondence: wangbo@stanford.edu

Summary

Animal behavior emerges from collective dynamics of interconnected neurons, making it vulnerable to connectome damage. Paradoxically, many organisms maintain significant behavioral output after large-scale neural injury. Molecular underpinnings of this extreme robustness remain largely unknown. Here, we develop a quantitative behavioral analysis pipeline to measure previously uncharacterized long-lasting latent memory states in planarian flatworms during whole-brain regeneration. By combining >20,000 animal trials with neural population dynamic modeling, we show that long-range volumetric peptidergic signals allow the planarian to rapidly reestablish latent states and restore coarse behavior after large structural perturbations to the nervous system, while small-molecule neuromodulators gradually refine the precision. The different time and length scales of neuropeptide and small-molecule transmission generate incoherent patterns of neural activity which competitively regulate behavior and memory. Controlling behavior through opposing communication mechanisms creates a more robust system than either alone and may serve as a generic approach to construct robust neural networks.

Introduction

Given its high interconnected complexity, the nervous system is expected to be vulnerable to major neuronal losses such as injuries, stroke, and degeneration[1,2]. However, many animals are capable of regenerating large sections of their nervous system after severe injury while maintaining high levels of motor function and sensitivity to various stimuli[3–7]. The extreme robustness of their nervous system allows them to sense and escape from harmful environmental cues such as predators and UV irradiation even during the process of regrowing a head. Neural robustness is generally thought to be built in the topology of synaptic connectome using redundant links to remove nodes of high centrality and reduce dependency on any given neuron[1,2,8–10]. Examples include distributed nerve nets of cnidarians[3,4] and duplicated neural circuits in segmented animals such as annelids and insects[5,6]. However, the duplication of network components may be limited by the high metabolic cost of neural maintenance[11].

Here, we present evidence for an alternative strategy for neural robustness: in addition to synaptic connections, volumetrically transmitted long-range signals could increase effective connectivity of the network without adding new structures to the system (**Figure 1A**). Volume transmission is common in the nervous system and occurs at multiple scales. Besides transmitting across synapses, small molecules such as monoamines and acetylcholine can leak out of the synaptic cleft and function as neuromodulators. However, due to rapid reuptake and extracellular degradation, their diffusion is limited to fast timescales (~100 ms) and short distances (~μm), thereby targeting immediately adjacent neurons[12–14]. In contrast, neuropeptides can be secreted throughout the entire neuronal body and diffuse for up to minutes over hundreds of microns, transmitting their signal to potentially large numbers of neurons with matching receptors[15–17]. The large length scale of

3

48 neuropeptide communication and its independence from synaptic connections may reduce

49 sensitivity to disruptions like missing neurons, axons, or connections.

50

51 We demonstrate neural robustness based on long-range diffusion through both experimental and

52 computational model systems. Experimentally, we study the planarian flatworm *Schmidtea*

53 *mediterranea*, a basal cephalized animal with the ability to regenerate its entire nervous system

54 from small tissue fragments[18–22]. This regenerative ability is key to the survival and reproduction

55 of planarians, which undergo asexual fission by ripping off tail fragments which then develop into

56 new individuals[23]. The planarian nervous system contains diverse neural cell types and complex

57 structures including a bi-lobed brain, ventral nerve cords, and peripheral projections[24,25]. The

58 number of neurons may fluctuate between ~1,000 to ~100,000 in a single animal during growth

59 and degrowth, requiring dynamic scaling of the entire neural architecture[18]. At the functional level,

60 planarians show complex behavior that integrates information from chemical, light, temperature,

61 and mechanical stimuli[26]. In particular, ultraviolet (UV) light and mechanical cues are detected

62 through sensory cells distributed throughout the body and can stimulate reflex-like responses in

63 decapitated animals[7,27,28], though it is unclear whether more complex behaviors such as sensory

64 integration are similarly independent of the brain. The cellular and molecular underpinnings of the

65 planarian's behavioral robustness remain mostly unexplored.

66

67 By developing a long-term high-content imaging platform, we observed thousands of planarians

68 during homeostasis and regeneration and quantified their behavior through six orders of magnitude

69 in time. This allowed us to identify previously unknown behavior including signal integration and

70 short-term memory, which revealed a long-lasting latent state in the planarian nervous system. We

71 discovered that maintenance of this excited state is mediated by neuropeptides and demonstrably

72 more robust than inhibition, which is controlled by locally-acting small-molecule

73 neurotransmitters. Using a dual-channel neural signaling model, we show that the different time

74 and length scales of neuropeptide and small-molecule transmission create interfering patterns of

75 neural activity which competitively control neural population dynamics. Though genetic and

76 surgical structural network disruptions perturb both transmission mechanisms, long-range

77 diffusion allows peptide-mediated dynamics to better persist than those driven by small-molecules.

78 This allows peptide function to dominate, generating robust behavioral output. By dynamically

79 balancing contributions of the two signaling mechanisms, this mode of 'adaptive robustness'

80 achieves more consistent control after injury than either system would alone.

81

82 **Results**

83 **High-content imaging reveals an excitable latent state in the planarian behavior**

84 To uncover complex behavior of planarians such as sensory integration and memory, we imaged

85 freely behaving planarians for extended periods, which has been challenging due to their strong

86 preference for solid edges and photophobic responses[29]. We developed quasi-2D fluidic

87 chambers[30] to contain animals (**Figure 1B**) and used infrared (IR) for non-perturbative

88 illumination[31,32]. We also incorporated programmable UV (365 nm) and vibrational stimuli to

89 drive ecologically relevant behavior through distinct sensory pathways[26–28,33]. We confirmed that

90 planarians could be continuously imaged on this setup over multiple days without significant

91 changes to their behavior (**Figure S1**).

92

93 Continuous imaging with a sub-second resolution allowed us to track animals and quantify the

5

94   changes in their positions over time (i.e., speed). Additionally, we defined a scalar activity

95   measurement based on the rate of change in the planarian's shape (**Figure 1C**, see **Methods**). This

96   activity score differentiated gliding, turning, and twitching, whereas speed did not resolve the latter

97   two (**Figure 1D**, **Supplemental Movie 1**). Activity measurements enabled us to quantify

98   responses with high sensitivity and precision across a broad range of UV doses (**Figure S2**).

99   Beyond known immediate reflexes[7,27], short UV pulses (<10 s) resulted in exponentially decaying

100   post-stimulus activity, and longer stimulation caused persistent high activity for several minutes

101   before decay (**Figure 1E**). The duration of high activity extended proportional to the dose of

102   stimuli, implicating an ability to both integrate stimulus and differentiate the subsequent behavior

103   through maintenance of activity over several minutes and inhibition of responses at appropriate

104   end points. This led to a broad power-law scaling between pulse duration and total post-stimulus

105   activity, consistent with Steven's law[34] (**Figure S2A**).

106

Maintenance and inhibition of behavioral state exhibit differential robustness during neural

108   **regeneration**

109   This readout of minutes-long memory enabled us to study how planarian's information processing

110   ability changes during neural injury. We bisected planarians to completely remove the brain and

111   measured the UV response of tail fragments every two hours throughout regeneration (**Figure 1F**).

112   The response to long UV pulses (e.g., 30 s) remained largely intact, though with a reduction in

113   peak and total response after amputation. Strikingly, by 2 days post amputation (dpa), peak activity

114   was not only fully restored, but the response duration, measured as the time needed for activity to

115   return to the baseline, was maintained twice as long after the stimuli compared to whole-animal

116   controls, indicating an inability to properly inhibit behavior output. Excess activity (total activity

117   beyond that of the control) gradually decreased as regeneration progressed and disappeared at ~8

118   dpa. Response to shorter pulses (e.g., 5 s) followed a similar trend, with initially reduced responses,

119   excess activity appearing as a second 'resonant' post-stimulus peak during 4-6 dpa, and full

120   recovery at 8 dpa. Notably, brain regeneration occurs in a similar timeframe, with a primordial

121   brain forming at ~3 dpa and undergoing structural development over the following week[19–21].

122

123   Varying pulse duration between 1-30 s, we found that each stimulus generated reduced responses

124   on the first day after amputation, suggesting impaired ability to maintain post-stimulus activity.

125   Recovery of this ability caused excess activity to appear earlier during regeneration in response to

126   higher UV doses. In contrast, suppression of excess activity did not occur until ~7 dpa, with the

127   timing mostly independent of the UV dose (**Figure 1G**, **Figure S3**). The fact that maintenance and

128   inhibition of UV-stimulated behavior recover asynchronously in regeneration suggests that they

129   are controlled by separate neural processes which have different capacities to function within a

130   partial nervous system.

131

132   To test whether this phenomenon was specific to the UV-sensory circuit, we stimulated planarians

133   using mechanical vibration which is sensed orthogonally to UV[28]. The post-stimulus response to

134   vibration followed a similar dose-response scaling as UV (**Figure S4A,B**). Following amputation,

135   vibration responses showed the same phases of recovery: early in regeneration the response was

136   reduced, then rebounded beyond the whole-animal controls before converging to the baseline

137   (**Figure S4C**), implying that the progression of behavioral recovery is likely governed by changes

138   in post-sensory neurons.

139

140 **Peptidergic and small-molecule signals maintain and inhibit behavioral states respectively**

141 We next sought to identify the neural transmission systems controlling the activation, maintenance,

142 and inhibition of post-stimulus behavior. We began by disrupting the core SNARE complex,

143 including *syntaxin*, *synaptobrevin*, and *snap25*, which mediates synaptic vesicle fusion and

144 release[35]. These RNAi experiments all resulted in loss of the UV response (**Figure 2A**),

145 demonstrating that the synaptic network is required for producing behavioral output in planarians.

146 In addition, RNAi of the vesicular glutamate transporter, *vglut*, severely reduced UV response

147 (**Figure 2B**) and caused uncoordinated movement (**Supplemental Movie 2**), suggesting that

148 glutamate is a key synaptic transmitter in planarians.

149

150 We reasoned that regulation of behavioral states on the minute time scale may be governed by

151 neuromodulators shifting the patterns of neural firing. We used RNAi to knock down synthesis

152 enzymes of various small-molecule neurotransmitters/neuromodulators and neuropeptides and

153 found that disruption of octopamine (i.e., tyramine beta-hydroxylase, *tbh*, RNAi), dopamine

154 (tyrosine hydroxylase, *th*), GABA (gabaergic decarboxylase, *gad*), and acetylcholine (choline

155 acetyltransferase, *chat*) syntheses all led to excess post-stimulus activity in response to UV. Similar

156 to the excess activity observed during regeneration, these knockdowns resulted in a second

157 resonant peak in activity after 5 s UV stimulation and a significantly delayed decay of activity after

158 30 s UV pulses (**Figure 2C,D**). *chat* RNAi also increased peak activity. This suggests that

159 inhibition of post-stimulus activity depends on the cumulative function of multiple small-molecule

160 neurotransmitters.

161

162 In contrast, reduction of post-stimulus activity was only observed when knocking down

163   prohormone convertase 2 (*pc2*), which is required for the maturation of many planarian

164   neuropeptides[36]. Planarians have densely packed peptidergic neurons collectively expressing a

165   suite of >60 neuropeptides, most, if not all, of which are also capable of generating small-molecule

166   neurotransmitters[24,36,37]. Long-range peptide transmission could create a densely connected

167   network as almost every planarian neuron expresses some neuropeptides or neuropeptide

168   receptors[24]. While peptides are known to often act synergistically[38,39], disrupting *pc2* allows for

169   reduction of overall peptide concentrations[36,40].

170

171   Though previous work noted that *pc2* knockdown severely reduces coordinated movement[41], we

172   found that *pc2* RNAi animals under continuous UV stimulation could activate the full range of

173   behavior seen in control animals (**Figure 2E**, **Supplemental Movie 3**). Consistently, their

174   response to UV stimuli was activated to levels matching that of controls and showed little

175   differences with weak stimuli. However, unlike controls that maintained high activity after long

176   stimulation (30 s), responses in *pc2* knockdown animals decayed immediately (**Figure 2F,G**). This

177   prevented the animals from differentiating their responses to long stimuli and caused saturation in

178   the dose-response curve (**Figure 2H**). These observations suggest that, while *pc2* RNAi animals

179   can detect and respond to UV, they fail to integrate signals and maintain the latent memory state

180   needed for extended post-stimulus activity. Concordantly, when we amputated *pc2* knockdown

181   animals, they failed to show either an extended response or resonant peak after 30 s and 5 s UV

182   pulses, respectively, during regeneration (**Figure 2I**). Altogether, these results suggest that long-

183   range peptide signaling underlies the rapid return of response maintenance after injury, whereas

184   small-molecule signals mediate the more fragile inhibitory functions.

185

Neuropeptide signaling maintains short-term memory

We hypothesized that other forms of memory at this timescale may also be mediated by peptides and similarly robust to injury. To test this, we exposed planarians to pairs of 5 s UV pulses separated by a time delay. With delays on the order of minutes, the response to the second pulse is significantly stronger than that of the first (**Figure 3A**), demonstrating sensitization, a form of short-term memory. This could be enhanced by stronger first pulses (**Figure 3B**). To measure how the memory of the first pulse changes over time[42], we varied the delay between pulses and found a non-monotonic decay of the sensitizing effect with a secondary peak at ~ 3 min delay (**Figure 3C**). Sensitization is also seen when pairing mechanical vibration and UV pulses, suggesting that this memory is embedded in post-sensory processes (**Figure 3D**).

While *pc2* RNAi did not affect response to single 5 s UV pulses (**Figure 2E**), it eliminated sensitization, indicating that neuropeptides are required for maintaining short-term memory (**Figure 3E**). Sensitization was initially lost in amputated planarians, but rapidly increased beyond that of whole animal controls at 1 dpa, demonstrating rapid recovery of sensitization memory but a lack of inhibition (**Figure 3F,G**). This observation parallels the trend in the single-pulse responses during regeneration, suggesting that the same peptide-dependent excitable latent state may encode both signal integration and short-term memory.

Peptide mediated functions are more robust to general brain perturbations

If long-range neuropeptide transmission is less reliant on the intact network structure than small-molecule signaling, then lost inhibition and excess behavioral activity should be a generic signature of brain injuries. To test this prediction, we performed several surgical cuts causing

10

209   partial brain damage, including severing anterior commissures (i.e., 'corpus callosum cut'),

210   amputating anterior to the eyespots, and biopsying posterior to the left eyespot. Even though these

211   injuries affected different neural structures, they all led to similarly extended UV responses within

212   the first day after injury (**Figure 4A**).

213

214   To rule out the possibility that excess activity is driven by wound response, we also perturbed

215   neural structures genetically by performing RNAi to disrupt a set of 9 transcription factors (TFs)

216   known to play important roles in the development of various neuronal populations and other

217   processes during brain regeneration such as patterning and size regulation[20–22,24,43]. Despite the

218   distinct functions of these TFs, almost all knockdowns led to similar excess activity in response to

219   UV through extended durations and higher activity peaks without physical injury (**Figure 4B,C**,

220   **Figure S5**). The strikingly consistent effect across surgical and genetic perturbations implies that

221   the differential robustness of maintenance and inhibition of the latent state is likely not caused by

222   asynchronous regeneration of controlling neural populations. Instead the two processes may be

223   encoded through distinct patterns in population-scale neural dynamics, with peptide-mediated

224   dynamics more robust to structural changes independent of specific neural circuits.

225

226   **Long-range volumetric transmission explains the robustness of peptide signaling**

227   We then asked whether differential signaling ranges are sufficient to explain the observed

228   difference in the robustness of peptide and small-molecule mediated processes. To do so we

229   developed a neural network model in which neurons interact through both volumetric and synaptic

230   signals and constrained the two systems to regulate behavior in the same manner seen in planarians.

231   We then tested whether these mechanistic underpinnings were sufficient to stabilize peptide

11

232   communication and generate excess behavioral output upon neural injury.

233

234   Specifically, we modeled population-scale neural dynamics using a custom recurrent neural

235   network (RNN) which simulates neuronal firing coupled through sparse synaptic links and

236   produces behavioral output through a readout matrix applied to the firing rates[44]. This model has

237   been previously shown to reproduce key aspects of animal neural dynamics when trained on

238   similar tasks[44–46]. To account for long-range volumetric signals, we augmented the model by

239   allowing neuron firing to trigger release of excitatory and inhibitory neuropeptides. These peptides

240   diffuse and persist extracellularly and modulate neuron firing potentials based on local

241   concentrations (**Figure 5A**, **Figure S6A**, see **Methods** for model details).

242

243   Because the model is implemented in a deep-learning framework, we were able to constrain its

244   dynamics to produce experimentally observed behavior. Simply training on wild type response is

245   insufficient to ensure that long-range peptide and targeted small-molecule signals in the model

246   maintain and inhibit behavioral activity, respectively. Therefore, we also trained on *pc2* RNAi data

247   while blocking peptide transmission in the model, allowing it to learn the effective contribution of

248   the volumetric signal.   Similarly, we trained on data of RNAi blocking small-molecule

249   transmission to constrain their functional roles. Because of the relatively fast and targeted scales

250   of small-molecule transmission, we model their contribution as instantaneous action through

251   synaptic links and assign subsets of neurons as octopaminergic, dopaminergic, GABAergic, and

252   cholinergic. When training on the RNAi data, transmission of the corresponding small molecule

253   was blocked while allowing neural firing and peptide release to sustain. This protocol was

254   sufficient to train models that each fit all the experiments simultaneously (**Figure 5B**).

255

256 We then tested whether these constraints were sufficient to explain the differential robustness of

257 the two communication mechanisms. We simulated the effects of neural injury by ablating regions

258 of neurons at various locations and sizes (**Figure 5C**-**E**). Matching experiments, large ablations

259 reduced the response, corresponding with early regeneration time points after decapitation when

260 the network is highly disrupted. Moderate ablations led to an extension of the response like those

261 observed in partially regenerated animals (**Figure 1E-G**). For a more direct experimental

262 validation, we amputated planarians to remove increasingly larger anterior structures and

263 measured response to 30 s UV pulses at 1 dpa. We observed the same trend of progressive increases

264 of duration and total responses before loss of response with largest amputations (**Figure 5F**). This

265 consistency between experiments and model predictions demonstrates that the robustness of

266 peptide signaling and the early return of peptide-mediated maintenance of behavioral state after

267 injury can be explained solely by the difference in transmission mechanisms, regardless of the

268 circuit details.

269

270 **Adaptive robustness through incoherent signal competition**

271 This dual-channel model also allowed us to study why maintenance and inhibition of behavior

272 segregates by mechanism of neural transmission. For this, we measured how the two mechanisms

273 interact to drive neural population dynamics. Due to long decay time and long-range diffusion,

274 peptide signaling generates slowly varying, spatially correlated patterns of neural activity. In

275 contrast, targeted connections and local neural modulations produce rapidly changing, spatially

276 uncorrelated neural firing patterns. Because both mechanisms are broadly co-expressed in

277 planarian neurons[24], these different patterns of neural activity propagate in a shared medium.

13

278 Mechanistic differences of the two systems create incoherent correlation structures which

279 effectively compete for control over neural population dynamics. By aligning motor output to

280 components of neural dynamics driven by peptide signaling (e.g., spatially continuous patterns),

281 peptide function should stabilize and maintain behavior activity, while high-frequency targeted

282 signals disrupt these patterns, drive the neural activity to new states, and effectively inhibit

283 behavior activity (**Figure S6B**).

284

285 Upon ablation, propagation of small-molecule mediated signals were more severely disrupted,

286 reducing their competitive influence on firing patterns and increasing the relative contribution of

287 neuropeptides. This effect could be quantified by the peptide-mediated spatial correlation in firing

288 dynamics, which became more pronounced after moderate ablations, explaining the excess

289 behavior seen in this regime (**Figure 5G**). This creates a system of behavior regulation through

290 neural pattern competition that is largely independent of specific neural circuitry, providing a new

291 paradigm of adaptive robustness during massive structural changes.

292

293 To further validate that differential robustness between signaling mechanisms drives the adaptive

294 robustness phenomenon, we varied the topological robustness of synaptic connectivity by training

295 over 150 independent RNN models with different connectivity network structures (**Figure S6C**).

296 More robust synaptic networks maintained their contribution to neural dynamics and prevented

297 ablation-induced excess activity even though the peptide transmission was kept identical (**Figure**

298 **5H**). This provides direct evidence that the excess activity induced by neural injury is caused by

299 the different capacity of the peptidergic and small-molecule signaling to maintain their functions

300 in disrupted neural networks.

301

302 **Discussion**

303 In this study, we used the planarian's ability to regrow an entire head de novo to study the neural

304 processes underlying its robust behaviors during brain regeneration. Extensive behavioral data and

305 computational analysis using a dual-channel signaling network led us to a conceptual model of

306 adaptive neural robustness (**Figure 6**). During structural injury, both channels are perturbed in a

307 correlated manner, making their competitive output, i.e., difference in strength, more robust than

308 the function of either alone. As the animal regenerates after injury, peptide-based functions recover

309 quickly due to the capacity of long-range diffusion to cross disrupted regions. In contrast, targeted

310 small-molecule functions require more complete connectome and thus take much longer to return.

311 By aligning behavioral output with the more robust peptide-dominant patterns of neural activity,

312 the planarian ensures reliable motor sensory responses throughout massive neural remodeling.

313

314 In contrast to neurogenesis during embryonic development that occurs in protected environments

315 such as an egg, neural regeneration must proceed while responding to threats from the surrounding

316 world. For example, protection from UV irradiation is critical as it induces DNA damage, which

317 can become particularly harmful during regeneration due to elevated cell proliferation[47].

318 Allocating functions activating strong UV responses to a relatively robust communication

319 mechanism allows for rapid re-establishment of key survival mechanisms like the escape response

320 while permitting other features to be re-established later. Short-term memory also provides a

321 means for animals to evaluate changes in stimuli across space and time. This can enable phototaxis

322 at length scales much larger than their body size[48,49], which is essential for planarians to locate

323 areas of lower exposure to minimize damage induced by UV. Our results demonstrate that short-

15

324   term memory is also mediated by neuropeptides allowing for recovery very early during

325   regeneration. Together, our findings imply that mechanisms enabling rapid behavioral recovery

326   after injury can provide an advantage under selective pressures in regenerating animals, especially

327   in organisms that reproduce through repeated fission and regeneration.

328

329   The long-range diffusion and slow time scales of neuropeptide signaling offer a molecular basis

330   for long-lasting latent neural states[50,51], which need to be robust after injury in order to properly

331   process information and maintain behavioral output. Indeed, the usage of peptide signals to

332   stimulate behaviors and promote arousal states has been observed in diverse animals including

333   nematodes, flies, and even mammals[15,52–54]. In some cases, it has been shown that the peptide-

334   dependent circuits function opposingly to synaptic connectome such that the interactions between

335   the two drive the switching between behavioral states[15,55]. The parallel across different organisms

336   implies that the division of labor between the two transmission mechanisms may be a common

337   feature of many neural circuits. Examining whether these circuits possess similarly high robustness

338   is an important avenue for future research.

339 **STAR Methods**

340

341 **RESOURCE AVAILABILITY**

342 *Lead Contact*

343 Further information and requests for resources and reagents should be directed to and will be

344 fulfilled by the lead contact, Bo Wang (wangbo@stanford.edu).

345

346 *Materials availability*

347 This study did not generate new unique reagents.

348

349 *Data and code availability*

350 All activity data used for analysis and model training are available at

351 tinyurl.com/robustBehavior. Original videos and radial segmentation measurements are available

352 from the authors upon request, due to the lack of public repository to host such large volumes of

353 data.

354

355 Software for video segmentation is available at github.com/samuelbray32/planameterization.

356 Repository for data analysis and visualization is available at github.com/samuelbray32/PARK.

357 Repository for dual-channel RNN model construction and training is available at

358 github.com/samuelbray32/dualChannelRNN.

359

360 **EXPERIMENTAL MODEL AND SUBJECT DETAILS**

361 *Animals*

17

362   Asexual *S. mediterranea* were maintained in the dark at 20 °C in water supplemented with 0.5 g/L

363   Instant Ocean Sea Salts (Carolina Biological Supply, Cat#671442) and 0.1 g/L sodium

364   biocarbonate. Planarians of ~4 mm in length were used for whole-animal behavior experiments

365   and were fed once or twice a week. For amputation experiments, we selected animals of ~8 mm in

366   length such that the regenerated fragments were approximately the same size as those used in

367   whole-animal experiments.

368

369   ***RNAi***

370   Gene knockdowns were carried out by feeding double-stranded RNA (dsRNA) to induce RNAi

371   mediated gene silencing. For all experiments, we fed dsRNA to animals 5-7 times every 4-5 d,

372   except *pc2* for which we fed 3 times. Animals were starved for 4 d prior to amputation, after which

373   tails were allowed to regenerate and imaged at 10-20 dpa, except for *pc2* RNAi animals, which

374   were imaged 5 d after the last feeding without amputation. Knockdown of *synaptobrevin* and

375   *syntaxin* caused lysis after ~20 dpa, but no gross morphological phenotypes were observed during

376   the time window of imaging.

377

378   The dsRNA was synthesized using the established protocol[36] and fed to animals by mixing in a

379   liver homogenate at a concentration of approximately 100 ng/µl. All clones for dsRNA synthesis

380   were generated using oligonucleotide primers (**Supplemental Table 1**) and cloned into vector

381   pJC53.2 (Addgene plasmid ID: 26536)[36]. For the RNAi control condition, we fed dsRNA matching

382   the ccdB and camR-containing insert of pJC53.2 under the same schedule of *pc2* RNAi. Results

383   from these experiments showed no significant difference from animals without RNAi feedings. To

384   maximize statistical power, we therefore combined data from these two conditions as the control

18

385   to compare against all other knockdown conditions.

386

387   **METHOD DETAILS**

388   *Imaging chamber*

389   To create the imaging chambers, 150 mm petri dishes were plasma treated (Harrick Plasma, PDC-

390   001) for 2 min at high power to create a hydrophilic surface. Ten circular templates with 20 mm

391   diameter were traced in each dish with a permanent marker to pattern a hydrophobic mask. Each

392   region was first loaded with a single planarian in 800 µl of Instant Ocean water to ensure complete

393   wetting and then reduced to ~350 µl. This flattened the top surface of the droplet and reduced

394   reflections during imaging. After loading, the dish was gently filled with ~50 mL of silicone oil

395   (Fisher Scientific S159-500) until the top of all droplets were covered. The oil phase both reduced

396   evaporation and increased surface tension at the droplet boundary to prevent planarians from

397   escaping. Planarians remained viable and active for at least ~7 d at 20 °C under these conditions.

398   All animals were starved at least 4 d prior to imaging and all imaging sessions lasted no longer

399   than 7 d. For imaging regeneration time courses, animals were loaded at 8 hpa and rinsed before

400   loading to reduce the accumulation of material ejected from the wound site within the droplet. To

401   cover the complete span of regeneration, a second cohort of animals was imaged starting 3 dpa for

402   ~7 days. Activity responses at matching regeneration time were merged from both datasets and

403   used for all analyses.

404

405   *Imaging setup*

406   Animals were illuminated with an IR light source (850 nm) from the side, and images were

407   recorded using a Rasberry Pi NoIR camera, except for a higher resolution camera (Daheng

19

408   Imaging, MER-1220-32U3M) used to generate the movies shown in **Supplemental Movie 1-2**.

409   UV light (365 nm) stimuli was delivered by a custom-built ring of 36 LEDs (Waveform Lighting,

410   7021.65) mounted above the camera to illuminate the entire dish uniformly and controlled by an

411   Arduino Uno (A000066) to adjust intensity and pulse duration. To eliminate glare from the

412   stimulus light source, an 800 nm long-pass filter (ThorLabs, FELH0800) was mounted within the

413   camera tube. Tactile stimulation was delivered by vibrating the stage with a small motor (Vibronics

414   Inc, VJQ24-35F580C), which was also controlled by the Arduino. For all stimulation experiments,

415   repetitions of the stimulation protocols were separated by 2 hr of unstimulated time to prevent

416   influence between trials.

417

418   ***Dual-channel RNN model***

419   We modified a well-established RNN model[44] by adding long-range volumetric signals. All neural

420   models were implemented, trained, and run using Keras architecture with Tensorflow 1.14

421   backend in a Python environment with CUDA GPU acceleration[56]. For a graphical diagram of

422   model architecture, see **Figure S6A**.

423

424   Models trained within this work contain 2500 neuron nodes arranged in a 50×50 square grid

425   (n_{neuron}) and 2 neuropeptides (n_{pep}). These values were chosen to maximize flexibility in model

426   training while maintaining loss gradients that could be stored in working memory. The RNN cell

427   has 5 state tensors passed between timepoints: a n_{neuron} vector of neuron states (X_{syn}), an array

428   of each neuropeptide concentration at each neuron location (X_{pep}), a binary variable indicating

429   whether neurons are capable of responding to neuropeptides in the sample condition (g_{pep}), a

430   vector describing the modulatory potency of each neuron in the sample condition (g_{syn}), and a

431   vector describing the ablation status of each neuron (A).

432

433   The model has one fixed parameter, a $n_{neuron} \times n_{neuron}$ connectivity matrix (C), which is a

434   sparse, binary matrix. This matrix is defined using the Watts-Strogatz method[57]. By varying the

435   average node-degree (k) and rewiring probability (β), this method can create networks with

436   topologies ranging from a completely regular ring structure ($\beta = 0$), to small-world networks ($0 <$

437     $\beta < 1$), to a random network ($\beta = 1$). As previous studies have demonstrated 'rich club' small-

438   world networks in a variety of neural systems[58], we defaulted to using a network with $k = 8$, $\beta =$

439   0.001. For the models shown in **Figure 5h**, triplicate models with different initializations and C

440   were trained with node degrees logarithmically spaced from 2 to 64, and β logarithmically spaced

441   from 0 to 1 to average the effects of the sparse weighted connections. To compare the robustness

442   of the synaptic connectivity topology, we calculated the graph connectivity of the network using

443   the python package NetworkX[59]. This measure describes the smallest number of nodes that must

444   be removed to separate the graph and corresponds with our simulated perturbation of node

445   ablation.

446

447   The RNN cell has 7 trainable model parameters: a $n_{simulus} \times n_{neuron}$ input vector transforming

448   stimulus condition into influence on the neuron states, a $n_{neuron} \times n_{neuron}$ weight matrix (W_{syn}),

449   a decay rate of neuron potential (δ_{neuron}), the production rate of each neuropeptide upon neuron

450   firing (μ_{pep}), the decay rate of each extracellular neuropeptide (δ_{pep}), the diffusivity of each

451   neuropeptide (D), the scaling coefficient of peptide action on local neuron potential (W_{pep}), and a

452   n_{neuron} vector W_{in} which defines the transformation of the current stimulus state (U_t) into change

453   in neuron potential.

21

454

455   At each time step, firing rates are sampled from the neuron state according to:

456    $$F = relu\left(X_{syn} + \mathcal{N}(0, 10^{-3})\right)$$

457   The non-linear rectifier maps the state of the cell into a positive firing rate[44]. Extracellular

458   neuropeptides are updated according to:

459    $$X_{pep}(t+1) = X_{pep}(t) + \mu_{pep}F - \delta_{pep}X_{pep}(t) + \mathcal{D}\left(X_{pep}(t), D\right)$$

460   where $\mathcal{D}$ applies a diffusivity kernel:

461    $$\mathcal{D}\left(X_{pep}(i,j,t), D\right) = D\left[-4X_{pep}(i,j,t) + X_{pep}(i-1,j,t) + X_{pep}(i+1,j,t) + \right.$$

462    $$\left. X_{pep}(i,j-1,t) + X_{pep}(i,j+1,t)\right]$$

463   to the peptide concentrations according to their arrangement on the square array of neurons. For

464   calculating spatial diffusion, the array is treated with periodic boundary conditions to remove the

465   effect of system size. Neural state updates are given by:

466    $$X_{syn}(t+1) = \left[X_{syn}(t) - \delta_{neuron}X_{syn}(t) + \left(W_{syn} \odot C\right)\left(g_{syn} \odot F\right) + W_{pep}\left(g_{pep} \odot \right.\right.$$

467    $$\left.\left. X_{pep}\right) + W_{in}U_t\right] \odot A.$$

468   Multiplication of modulatory weights and connectivity enforces a specific, sparse network of

469   connections throughout training. Multiplication of g_{syn} and the firing rate masks output from

470   genetic knockdown of small-molecules. Multiplication of g_{pep} and X_{pep} masks contribution of

471   neuropeptide signaling. Multiplication of the entire state with A completely masks all contributions

472   of ablated neurons in a sample.

473

474   Model inputs are the stimulus vector across the simulation time range U, g_{syn}, g_{pep}, and A, which

475   are concatenated in the model with X_0, a trainable variable providing the neuron and peptide states

22

476   at time zero within the RNN. This concatenated tensor is fed as initial conditions to the RNN. The

477   RNN then simulates 1,200 timesteps (10 min) of zero-stimulus response. This allowed the neuron

478   states in a sample to evolve to form a stable state, which is given the knockdown and ablation

479   input. The final equilibrated state is then passed with U to the RNN, which simulates the dynamics

480   and returns the complete neural state at each timepoint. This is rectified into the firing rate, and

481   convolved with a single time step kernel, which effectively applies a trainable output matrix W_{out}

482   to the firing rates at each time step to generate the simulated activity (Z). Z is returned as the output

483   of the complete machine learning model.

484

485   For initialization, elements in large weight matrices were independently sampled according to:

486    $W_{syn}(i,j) \sim \mathcal{N}(2 \times 10^{-5}, 2 \times 10^{-4})$, neural states of $X_0(i,j) \sim \mathcal{N}(0,10^{-2})$, peptide states of

487    $X_0(i,j) \sim Exp(10^{-2})$, $W_{in}(i,j) \sim \mathcal{N}(0,5)$, and $W_{out}(i,j) \sim \mathcal{N}(0,0.05)$. Other parameters were set

488   to: $\mu_{pep} = [1,1]$, $\delta_{pep} = [0.2,0.2]$, $D = [3,10]$, $W_{pep} = [0.9,-0.6]$, $\delta_{neuron} = 1.25$. These values

489   were chosen to produce non-diverging neural dynamics from which to begin training.

490

491   Models were trained on the median activity. To prevent overfitting to the timing of the UV pulse

492   during the simulation, the training data contained 20 samples for each stimulation and knockdown

493   condition with start times randomly selected between 1-4 min before the start of stimulation and a

494   sample duration of 26 min (except for Era 1, in which duration was set to 13 min to reduce size of

495   gradient operations and speed the initial training to obtain a rough shape of the response). The

496   training was performed without ablation ($A = 1$). In samples of *pc2* RNAi data, $g_{pep} = 0$. To

497   account for small-molecule neurotransmitter knockdowns, neurons were randomly assigned as

498   GABAergic (12.5%), octopaminergic (12.5%), dopaminergic (12.5%), or cholinergic (50%), or

23

499   generic (12.5%). The relatively high fraction of cholinergic neurons was chosen to match their

500   abundance in the planarian nervous system[24], but the model result was only weakly dependent on

501   the neuronal type fractions. We did not specify spatial patterns for these neuronal types to keep

502   the model general and mostly species agnostic. In samples of *gad*, *tbh*, *th*, or *chat* RNAi data, g_{syn}

503   was set to zero for the corresponding neurons to prevent their small-molecule modulatory

504   activities.

505

506   The loss ($\mathcal{L}$) was defined as the mean square error between the median activity and simulated

507   activity Z, and was optimized using ADAM gradient descent[60]. Models were trained in 4 eras:

508   Era 1: learning rate=$10^{-4} + 10^{-3} \exp\left(-\frac{epoch}{15}\right)$, epochs = 10, batch size = 6

509   Era 2: learning rate=$10^{-4} + 10^{-3} \exp\left(-\frac{epoch}{15}\right)$, epochs = 40, batch size = 4

510   Era 3: learning rate=3×10^{-5}, epochs=10, batch size = 4

511   Era 4: learning rate= $3 \times 10^{-5} + 10^{-4} \exp\left(-\frac{epoch}{3}\right)$, epochs = 10, batch size = 4

512   In Era 4, training was stopped early if the change in average loss was less than 5×10^{-4} for 3

513   consecutive epochs.

514

515   Each model was trained using responses to 5 s and 30 s pulses for control animals, as well as *pc2*,

516   *gad*, *tbh*, *th*, and *chat* RNAi animals. To further constrain the functional fitting within the model,

517   we performed double knockdowns of *gad:pc2*, *tbh:pc2*, *th:pc2*, and *chat:pc2* and included them

518   within the training set. Additionally, to stabilize the long-term behavior of the simulated model,

519   we stimulated animals with UV for 30 min at reduced intensities and included this data within the

520   training set.

521

522   After training, the rate parameters in the model shown in detail in **Figure 5** were: D: [2.9952657

523   10.002745]; μ_{pep} : [1.006925   0.99327475]; δ_{pep}: [0.2064426 0.19140989]; W_{pep}: [0.90302687,

524   -0.59036015]; δ_{neuron}: [1.2581608]. These parameters gave the range of peptide diffusion to be

525   3-10 cell bodies and their half-life to be ~ 5 min, which are biologically realistic based on previous

526   measurements[38].

527

528   To simulate responses after ablation, the ablation vector (A) was generated to mask out neurons

529   corresponding to a spatially contiguous rectangular region of minimum aspect ratio with the

530   desired fraction of neurons. The location of the ablated region within the array was randomly

531   chosen for each sample. For each ablation fraction, responses were generated from 200 different

532   ablated regions and averaged to remove dependencies on locations of the ablation.

533

534   The spatial covariance was calculated by averaging over all pairs of neurons at a given distance

535   and across all timepoints on simulations lasting 11 min with a single 3 s pulse. This was sufficient

536   to drive neural activity without dominating the signal with spatial correlation embedded within the

537   input matrix W_{in}. Ablated neurons were excluded from the calculation. For each ablation fraction,

538   we simulated results from 200 ablated regions and averaged covariances at each distance.

539

540   **QUANTIFICATION AND STATISTICAL ANALYSIS**

541   ***Behavioral activity quantification***

542   Planarians were segmented using binary thresholding. For each frame, the center of mass (COM)

543   of the animal was determined and the perimeter pixel locations were identified and interpolated to

25

544   give 100 evenly spaced anchor points. Radial distances were calculated as the distance from the

545   COM to each of these points. The radial measurement vector was L1 normalized and aligned such

546   that the maximum radial distance is at position 0. We then reduced the dimensionality of the radial

547   measurements using Principal Component Analysis (PCA) and used the first 10 PCs (97%

548   explained variance) for further analysis[61]. PCs calculated using data from intact animals

549   responding to 5 s UV stimulation were used to analyze all datasets. These PCs correspond to

550   'eigen-shapes' of the worm during movement, e.g., elongation (PC1), turning (PC2), and

551   scrunching (PC3)[61]. For PCs that are symmetric across the worm (e.g., turning left and right gives

552   positive and negative values on PC2 respectively[61]), we took the absolute value of the component

553   to prevent unnecessary separation of similar behaviors.

554

555   Because stationary and moving animals occupied overlapping shape space, incorporating temporal

556   information into the feature vector significantly improved our ability to quantify behavioral

557   activity. To do so, we convolved the shape measurement with Haar wavelet filters[62] at scales

558   corresponding to 2.5, 7.5, and 15 s to obtain the rate of shape change at each time point. This also

559   served to filter out noise from the segmentation steps. Finally, we fit a one-dimensional stochastic

560   linear dynamic system (LDS) model to the wavelet filtered data[63] using the state space models

561   (SSM) Python package[64]. This model is a continuous analogue of the discrete Hidden Markov

562   Model and infers a single latent scalar variable (activity) at each timepoint which maximizes the

563   likelihood of the observations (wavelet filtered data).

564

565   ***Statistical analysis***

566   Planarians displayed an asymmetric multimodal distribution of activities at any given time point.

567   Therefore, we used non-parametric bootstrap statistics to test for significant differences between

568   population averages. When comparing time trace data, each bootstrap sample was performed by

569   choosing n responses with replacement from the collected data, where n is the number of responses

570   within the given dataset (**Supplemental Table 2**). This created new samples matching the size of

571   the experimental dataset[65]. The median value from these samples at each timepoint was recorded.

572   This procedure was repeated >1000 times to form a sampling distribution of the median population

573   activity at each timepoint from 5 min before to 30 min after the stimulus. All time traces plotted

574   are the mean estimate of median activity with 99% confidence intervals (CIs).

575

576   To test for significant differences between two conditions (e.g., RNAi), paired sets of samples

577   were taken from each dataset and the difference in median activity between each sample was

578   recorded. This procedure was repeated to form a sampling distribution of the difference in median

579   activities at each timepoint. Significance at a time point was declared if zero falls outside the 99%

580   CI.

581

582   ***Response measurements***

583   To compare responses between conditions, we used three summary statistics. First, total response

584   was quantified as the average median population activity during 10 min post-stimulation. This

585   interval was sufficiently long to capture the dynamics of extended responses while maintaining

586   sensitivity to short pulses. Post-stimulus response duration was defined as the time at which the

587   median activity first fell below a threshold value, 0.3, after stimulation. This threshold was chosen

588   to lie above the confidence interval of unstimulated population activity. Peak response was

589   quantified by the maximum median activity after the end of stimulation. To compare these values

590   between conditions, we used non-parametric bootstrap estimation. We calculated the measurement

591   on 1,000 paired sample sets from control and experimental conditions and recorded the difference.

592   Significance was declared if zero difference fell outside the 99% confidence interval for the

593   sampling distribution of differences.

References

1. Bullmore, E., and Sporns, O. (2009). Complex brain networks: graph theoretical analysis of structural and functional systems. Nat. Rev. Neurosci. *10*, 186–198. 10.1038/nrn2575.

2. Aerts, H., Fias, W., Caeyenberghs, K., and Marinazzo, D. (2016). Brain networks under attack: robustness properties and the impact of lesions. Brain *139*, 3063–3083. 10.1093/brain/aww194.

3. Dupre, C., and Yuste, R. (2017). Non-overlapping neural networks in Hydra vulgaris. Curr. Biol. *27*, 1085–1097. 10.1016/J.CUB.2017.02.049.

4. Weissbourd, B., Momose, T., Nair, A., Kennedy, A., Hunt, B., and Anderson, D.J. (2021). A genetically tractable jellyfish model for systems and evolutionary neuroscience. Cell *184*, 5854-5868.e20. 10.1016/J.CELL.2021.10.021.

5. Yasui, K., Kano, T., Standen, E.M., Aonuma, H., Ijspeert, A.J., and Ishiguro, A. (2019). Decoding the essential interplay between central and peripheral control in adaptive locomotion of amphibious centipedes. Sci. Rep. *9*, 1–11. 10.1038/s41598-019-53258-3.

6. Lybrand, Z.R., and Zoran, M.J. (2012). Rapid neural circuit switching mediated by synaptic plasticity during neural morphallactic regeneration. Dev. Neurobiol. *72*, 1256–1266. 10.1002/DNEU.20993.

7. Le, D., Sabry, Z., Chandra, A., Kristan, W.B., and Collins, E.M.S. (2021). Planarian fragments behave as whole animals. Curr. Biol. *31*, 5111-5117.e4. 10.1016/J.CUB.2021.09.056.

8. Li, N., Daie, K., Svoboda, K., and Druckmann, S. (2016). Robust neuronal dynamics in premotor cortex during motor planning. Nature *532*, 459–464. 10.1038/nature17643.

9. Hillary, F.G., and Grafman, J.H. (2017). Injured brains and adaptive networks: The

617   benefits and costs of hyperconnectivity. Trends Cogn. Sci. *21*, 385–401.

618   10.1016/J.TICS.2017.03.003.

619 10. Miranda-Dominguez, O., Mills, B.D., Grayson, D., Woodall, A., Grant, K.A., Kroenke,

620   C.D., and Fair, D.A. (2014). Bridging the gap between the human and macaque

621   connectome: A quantitative comparison of global interspecies structure-function

622   relationships and network topology. J. Neurosci. *34*, 5552–5563.

623   10.1523/JNEUROSCI.4229-13.2014.

624 11. Niven, J.E., and Laughlin, S.B. (2008). Energy limitation as a selective pressure on the

625   evolution of sensory systems. J. Exp. Biol. *211*, 1792–1804. 10.1242/JEB.017574.

626 12. Nusbaum, M.P., Blitz, D.M., and Marder, E. (2017). Functional consequences of

627   neuropeptide and small-moleculeco-transmission. Nat. Rev. Neurosci. *18*, 389.

628   10.1038/NRN.2017.56.

629 13. Hille, B. (1992). G protein-coupled mechanisms and nervous signaling. Neuron *9*, 187–

630   195. 10.1016/0896-6273(92)90158-A.

631 14. Fuxe, K., Dahlström, A.B., Jonsson, G., Marcellino, D., Guescini, M., Dam, M., Manger,

632   P., and Agnati, L. (2010). The discovery of central monoamine neurons gave volume

633   transmission to the wired brain. Prog. Neurobiol. *90*, 82–100.

634   10.1016/J.PNEUROBIO.2009.10.012.

635 15. Flavell, S.W., Pokala, N., Macosko, E.Z., Albrecht, D.R., Larsch, J., and Bargmann, C.I.

636   (2013). Serotonin and the neuropeptide PDF initiate and extend opposing behavioral states

637   in *C. elegans*. Cell *154*, 1023–1035. 10.1016/J.CELL.2013.08.001.

638 16. Brewer, J.C., Olson, A.C., Collins, K.M., and Koelle, M.R. (2019). Serotonin and

639   neuropeptides are both released by the HSN command neuron to initiate *Caenorhabditis*

640   *elegans* egg laying. PLoS Genet. *15*, e1007896. 10.1371/JOURNAL.PGEN.1007896.

641   17.   Van den Pol, A.N. (2012). Neuropeptide transmission in brain circuits. Neuron *76*, 98.

642   10.1016/J.NEURON.2012.09.014.

643   18.   Cebrià, F. (2007). Regenerating the central nervous system: How easy for planarians!

644   Dev. Genes Evol. *217*, 733–748. 10.1007/S00427-007-0188-6/FIGURES/6.

645   19.   Evans, D.J., Owlarn, S., Romero, B.T., Chen, C., and Aboobaker, A.A. (2011).

646   Combining classical and molecular approaches elaborates on the complexity of

647   mechanisms underpinning anterior regeneration. PLoS One *6*, e27927.

648   10.1371/JOURNAL.PONE.0027927.

649   20.   Brown, D.D.R., Molinaro, A.M., and Pearson, B.J. (2018). The planarian TCF/LEF factor

650   Smed-tcf1 is required for the regeneration of dorsal-lateral neuronal subtypes. Dev. Biol.

651   *433*, 374–383. 10.1016/j.ydbio.2017.08.024.

652   21.   Roberts-Galbraith, R.H., Brubacher, J.L., and Newmark, P.A. (2016). A functional

653   genomics screen in planarians reveals regulators of whole-brain regeneration. Elife *5*,

654   e17002. 10.7554/eLife.17002.

655   22.   Currie, K.W., Molinaro, A.M., and Pearson, B.J. (2016). Neuronal sources of hedgehog

656   modulate neurogenesis in the adult planarian brain. Elife *5*, e19735. 10.7554/eLife.19735.

657   23.   Vila-Farré, M., and Rink, J.C. (2018). The ecology of freshwater planarians. Methods

658   Mol. Biol. *1774*, 173–205. 10.1007/978-1-4939-7802-1_3.

659   24.   Wyss, L.S., Bray, S.R., and Wang, B. (2022). Cellular diversity and developmental

660   hierarchy in the planarian nervous system. Curr. Opin. Genet. Dev. *76*, 101960.

661   10.1016/j.gde.2022.101960.

662   25.   Ross, K.G., Currie, K.W., Pearson, B.J., and Zayas, R.M. (2017). Nervous system

663   development and regeneration in freshwater planarians. Wiley Interdiscip. Rev. Dev. Biol.

664   *6*, e266. 10.1002/WDEV.266.

665 26. Inoue, T., Hoshino, H., Yamashita, T., Shimoyama, S., and Agata, K. (2015). Planarian

666   shows decision-making behavior in response to multiple stimuli by integrative brain

667   function. Zool. Lett. *1*, 7. 10.1186/s40851-014-0010-z.

668 27. Shettigar, N., Chakravarthy, A., Umashankar, S., Lakshmanan, V., Palakodeti, D., and

669   Gulyani, A. (2021). Discovery of a body-wide photosensory array that matures in an

670   adult-like animal and mediates eye-brain-independent movement and arousal. Proc. Natl.

671   Acad. Sci. *118*, e2021426118.

672   10.1073/PNAS.2021426118/SUPPL_FILE/PNAS.2021426118.SM05.MOV.

673 28. Ross, K.G., Molinaro, A.M., Romero, C., Dockter, B., Cable, K.L., Gonzalez, K., Zhang,

674   S., Collins, E.M.S., Pearson, B.J., and Zayas, R.M. (2018). SoxB1 activity regulates

675   sensory neuron regeneration, maintenance, and function in planarians. Dev. Cell *47*, 331-

676   347.e5. 10.1016/J.DEVCEL.2018.10.014.

677 29. Akiyama, Y., Agata, K., and Inoue, T. (2015). Spontaneous behaviors and wall-curvature

678   lead to apparent wall preference in planarian. PLoS One *10*, e0142214.

679   10.1371/JOURNAL.PONE.0142214.

680 30. Soitu, C., Feuerborn, A., Tan, A.N., Walker, H., Walsh, P.A., Castrejón-Pita, A.A., Cook,

681   P.R., and Walsh, E.J. (2018). Microfluidic chambers using fluid walls for cell biology.

682   Proc. Natl. Acad. Sci. U. S. A. *115*, E5926–E5933.

683   10.1073/PNAS.1805449115/SUPPL_FILE/PNAS.1805449115.SM05.MP4.

684 31. Azuma, K., Iwasaki, N., and Ohtsu, K. (1999). Absorption spectra of planarian visual

685   pigments and two states of the metarhodopsin intermediates. Photochem. Photobiol. *69*,

686   99–104. 10.1111/J.1751-1097.1999.TB05312.X.

687   32.   Dexter, J.P., Tamme, M.B., Lind, C.H., and Collins, E.M.S. (2014). On-chip

688   immobilization of planarians for in vivo imaging. Sci. Rep. *4*, 6388. 10.1038/SREP06388.

689   33.   Shettigar, N., Joshi, A., Dalmeida, R., Gopalkrishna, R., Chakravarthy, A., Patnaik, S.,

690   Mathew, M., Palakodeti, D., and Gulyani, A. (2017). Hierarchies in light sensing and

691   dynamic interactions between ocular and extraocular sensory networks in a flatworm. Sci.

692   Adv. *3*, e1603025. 10.1126/SCIADV.1603025.

693   34.   Stevens, S.S. (1957). On the psychophysical law. Psychol. Rev. *64*, 153–181.

694   35.   Südhof, T.C. (2013). Neurotransmitter release: The last millisecond in the life of a

695   synaptic vesicle. Neuron *80*, 675–690. 10.1016/J.NEURON.2013.10.022.

696   36.   Collins, J.J., Hou, X., Romanova, E. V., Lambrus, B.G., Miller, C.M., Saberi, A.,

697   Sweedler, J. V., and Newmark, P.A. (2010). Genome-Wide analyses reveal a role for

698   peptide hormones in planarian germline development. PLoS Biol. *8*, e1000509.

699   10.1371/JOURNAL.PBIO.1000509.

700   37.   Khariton, M., Kong, X., Qin, J., and Wang, B. (2020). Chromatic neuronal jamming in a

701   primitive brain. Nat. Phys. *16*, 553–557. 10.1038/s41567-020-0809-9.

702   38.   Jékely, G., Melzer, S., Beets, I., Kadow, I.C.G., Koene, J., Haddad, S., and Holden-Dye,

703   L. (2018). The long and the short of it - A perspective on peptidergic regulation of circuits

704   and behaviour. J. Exp. Biol. *221*, jeb166710. 10.1242/JEB.166710/20346.

705   39.   Williams, E.A., Verasztó, C., Jasek, S., Conzelmann, M., Shahidi, R., Bauknecht, P.,

706   Mirabeau, O., and Jékely, G. (2017). Synaptic and peptidergic connectome of a

707   neurosecretory center in the annelid brain. Elife *6*, e26349. 10.7554/ELIFE.26349.

708   40.   Zhang, X., Pan, H., Peng, B., Steiner, D.F., Pintar, J.E., and Fricker, L.D. (2010).

709   Neuropeptidomic analysis establishes a major role for prohormone convertase-2 in

710   neuropeptide biosynthesis. J. Neurochem. *112*, 1168. 10.1111/J.1471-4159.2009.06530.X.

711 41. Reddien, P.W., Bermange, A.L., Murfitt, K.J., Jennings, J.R., and Sánchez Alvarado, A.

712   (2005). Identification of genes needed for regeneration, stem cell function, and tissue

713   homeostasis by systematic gene perturbation in planaria. Dev. Cell *8*, 635–649.

714   10.1016/J.DEVCEL.2005.02.014.

715 42. Liu, M., Sharma, A.K., Shaevitz, J.W., and Leifer, A.M. (2018). Temporal processing and

716   context dependency in caenorhabditis elegans response to mechanosensation. Elife *7*.

717   10.7554/ELIFE.36419.

718 43. Scimone, M.L., Kravarik, K.M., Lapan, S.W., and Reddien, P.W. (2014). Neoblast

719   specialization in regeneration of the planarian Schmidtea mediterranea. Stem Cell Rep. *3*,

720   339–352. 10.1016/J.STEMCR.2014.06.001.

721 44. Song, H.F., Yang, G.R., and Wang, X.J. (2016). Training excitatory-inhibitory recurrent

722   neural networks for cognitive tasks: A simple and flexible framework. PLoS Comput.

723   Biol. *12*, e1004792. 10.1371/JOURNAL.PCBI.1004792.

724 45. Vyas, S., Golub, M.D., Sussillo, D., and Shenoy, K. V. (2020). Computation through

725   neural population dynamics. Annu. Rev. Neurosci. *43*, 249–275. 10.1146/ANNUREV-

726   NEURO-092619-094115.

727 46. Yang, G.R., Joglekar, M.R., Song, H.F., Newsome, W.T., and Wang, X.J. (2019). Task

728   representations in neural networks trained to perform many cognitive tasks. Nat. Neurosci.

729   *22*, 297–306. 10.1038/s41593-018-0310-2.

730 47. Kapp, F.G., Perlin, J.R., Hagedorn, E.J., Gansner, J.M., Schwarz, D.E., O'connell, L.A.,

731   Johnson, N.S., Amemiya, C., Fisher, D.E., Wölfle, U., et al. (2018). Protection from UV

732   light is an evolutionarily conserved feature of the haematopoietic niche. Nature *558*, 445–

733   448. 10.1038/s41586-018-0213-0.

734   48.   Karpenko, S., Wolf, S., Lafaye, J., Le Goc, G., Panier, T., Bormuth, V., Candelier, R., and

735   Debrégeas, G. (2020). From behavior to circuit modeling of light-seeking navigation in

736   zebrafish larvae. Elife *9*, e52882. 10.7554/ELIFE.52882.

737   49.   Humberg, T.H., Bruegger, P., Afonso, B., Zlatic, M., Truman, J.W., Gershow, M.,

738   Samuel, A., and Sprecher, S.G. (2018). Dedicated photoreceptor pathways in *Drosophila*

739   larvae mediate navigation by processing either spatial or temporal cues. Nat. Commun. *9*,

740   1260. 10.1038/s41467-018-03520-5.

741   50.   Lim, M.A., Chitturi, J., Laskova, V., Meng, J., Findeis, D., Wiekenberg, A., Mulcahy, B.,

742   Luo, L., Li, Y., Lu, Y., et al. (2016). Neuroendocrine modulation sustains the *C. elegans*

743   forward motor state. Elife *5*, e19887. 10.7554/ELIFE.19887.

744   51.   Ma, S., Hangya, B., Leonard, C.S., Wisden, W., and Gundlach, A.L. (2018). Dual-

745   transmitter systems regulating arousal, attention, learning and memory. Neurosci.

746   Biobehav. Rev. *85*, 21–33. 10.1016/J.NEUBIOREV.2017.07.009.

747   52.   López-Cruz, A., Sordillo, A., Pokala, N., Liu, Q., McGrath, P.T., and Bargmann, C.I.

748   (2019). Parallel multimodal circuits control an innate foraging behavior. Neuron *102*, 407-

749   419.e8. 10.1016/J.NEURON.2019.01.053.

750   53.   Sehgal, A., and Mignot, E. (2011). Genetics of sleep and sleep disorders. Cell *146*, 194–

751   207. 10.1016/J.CELL.2011.07.004.

752   54.   Taylor, S.R., Santpere, G., Weinreb, A., Barrett, A., Reilly, M.B., Xu, C., Varol, E.,

753   Oikonomou, P., Glenwinkel, L., McWhirter, R., et al. (2021). Molecular topography of an

754   entire nervous system. Cell *184*, 4329-4347.e23. 10.1016/J.CELL.2021.06.023.

755   55.   Guillaumin, M.C.C., and Burdakov, D. (2021). Neuropeptides as primary mediators of

756   brain circuit connectivity. Front. Neurosci. *15*, 229.

757   10.3389/FNINS.2021.644313/BIBTEX.

758   56.   Abadi, M., Barham, P., Chen, J., Chen, Z., Davis, A., Dean, J., Devin, M., Ghemawat, S.,

759   Irving, G., Isard, M., et al. (2016). TensorFlow: A system for large-scale machine

760   learning. In Proceedings of the 12th USENIX Symposium on Operating Systems Design

761   and Implementation, pp. 265–278.

762   57.   Watts, D.J., and Strogatz, S.H. (1998). Collective dynamics of 'small-world' networks.

763   Nature *393*, 440–442. 10.1038/30918.

764   58.   Bentley, B., Branicky, R., Barnes, C.L., Chew, Y.L., Yemini, E., Bullmore, E.T., Vértes,

765   P.E., and Schafer, W.R. (2016). The multilayer connectome of Caenorhabditis elegans.

766   PLoS Comput. Biol. *12*, 1005283. 10.1371/journal.pcbi.1005283.

767   59.   Hagberg, Aric A; Schult, Daniel A; Swart, P.J. (2008). Exploring network structure,

768   dynamics, and function using NetworkX. In Proceedings of the Python in Science

769   Conference (SciPy), pp. 11–15.

770   60.   Kingma, D.P., and Ba, J. (2015). ADAM: A method for stochastic optimization. In 3rd

771   International Conference for Learning Representations.

772   61.   Werner, S., Rink, J.C., Riedel-Kruse, I.H., and Friedrich, B.M. (2014). Shape mode

773   analysis exposes movement patterns in biology: Flagella and flatworms as case studies.

774   PLoS One *9*, e113083. 10.1371/JOURNAL.PONE.0113083.

775   62.   Guan, J., Wang, B., and Granick, S. (2014). Even hard-sphere colloidal suspensions

776   display Fickian yet non-Gaussian diffusion. ACS Nano *8*, 3331–3336.

777   10.1021/NN405476T/SUPPL_FILE/NN405476T_SI_003.AVI.

778 63. Bishop, C.M. (2006). Pattern recognition and machine learning springer mathematical

779   notation Ni. In, pp. 635–647.

780 64. Antin, B., Zoltowski, D., Glaser, J., and Linderman, S. (2020). SSM: Bayesian learning

781   and inference for state space models.

782 65. Kulesa, A., Krzywinski, M., Blainey, P., and Altman, N. (2015). Sampling distributions

783   and the bootstrap. Nat. Methods *12*, 477–478. 10.1038/NMETH.3414.

792

793 **Author contributions.** Conceptualization: SRB, LSW, and BW; Methodology: SRB, LSW, CC,

794 and MEL; Investigation: SRB and LSW; Formal analysis: SRB; Validation: SRB and LSW;

795 Writing: SRB, LSW, and BW, with feedback from all other authors; Funding acquisition: BW;

796 Supervision: BW.
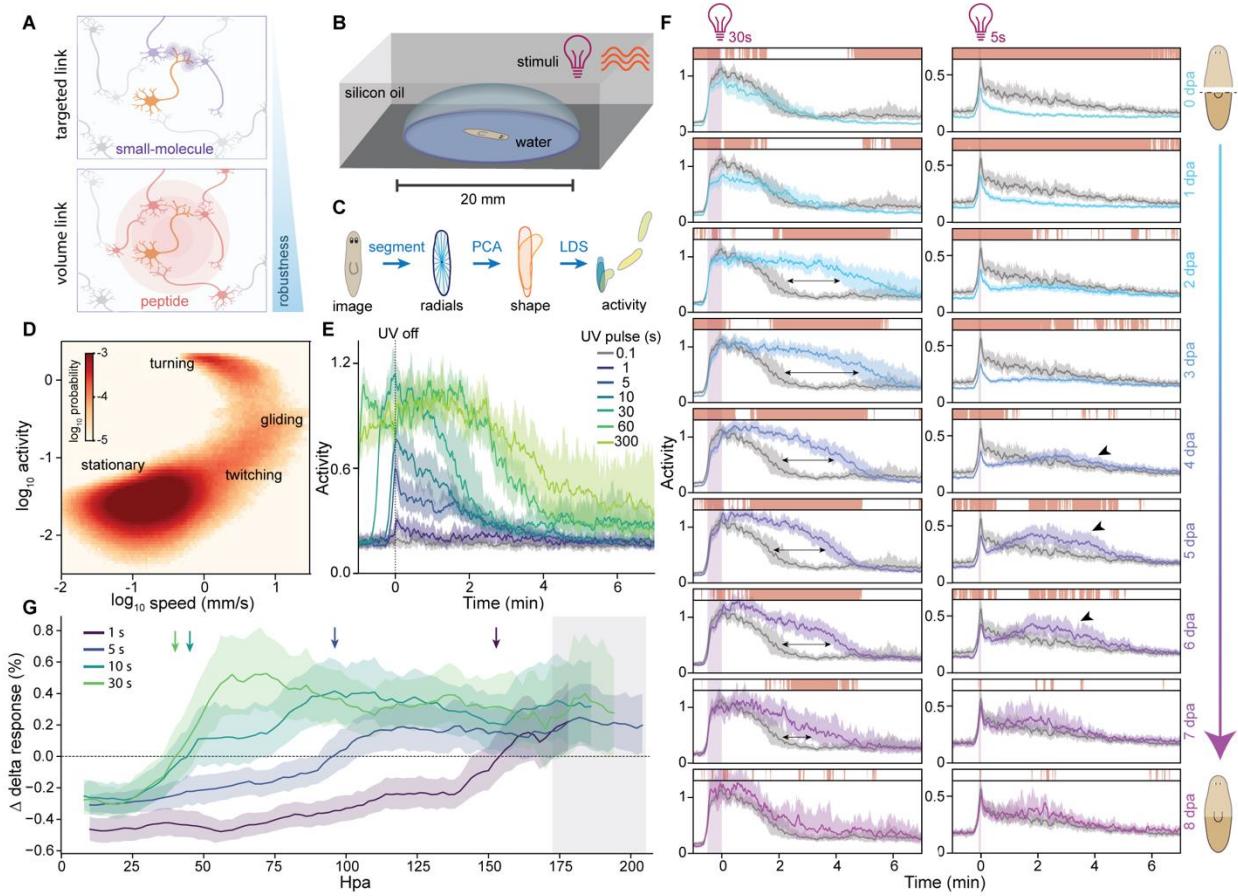
Figure 1: High-content imaging quantifies behavioral changes throughout regeneration.

(A) Schematic showing the different ranges of peptidergic and small-molecule signals. Neuropeptides create long-range volumetric diffusive cues that can increase robustness without the need to change synaptic network topology.

(B) Schematic showing the imaging setup with individual planarians recorded in separate aqueous droplets under IR illumination and UV or mechanical stimulations.

(C) Data processing pipeline includes segmentation, shape quantification using radial measurements, dimensional reduction through principal component analysis (PCA), and a linear dynamics system (LDS) to define the activity measurement.

(D) Joint distribution of activity and speed calculated from the behavioral data collected on animals under 5 s UV stimulation.

809   **(E)** Activity response of whole animals to UV stimuli ranging from 0.1 to 300 s. Time zero: end

810   of UV stimulation. For all time traces, solid lines: median activity; shaded region: 99% confidence

811   interval (CI).

812   **(F)** Response to UV stimulation throughout the time course of regeneration after decapitation.

813   Gray traces: whole-animal controls; colored traces: regenerating tail fragments. Purple bar:

814   duration of UV stimulation. Arrows: extended response to 30 s UV; arrowheads: 'resonant peak'

815   in response to 5 s UV. Bars above the traces indicate time when the response of regenerating

816   animals is significantly different from whole-animal controls as measured by 1,000 nonparametric

817   bootstrap comparisons of the two populations ($p < 0.01$). dpa: day post amputation.

818   **(G)** Fractional change in UV response during head regeneration relative to the whole-animal

819   control. Average responses are calculated by bootstrap sampling of data from 6 hr before to 6 hr

820   after every time point. Shaded region: 99% CI; arrows: end of reduced activity and beginning of

821   excess activity; grey shaded zone: end of excess activity. hpa: hour post amputation.
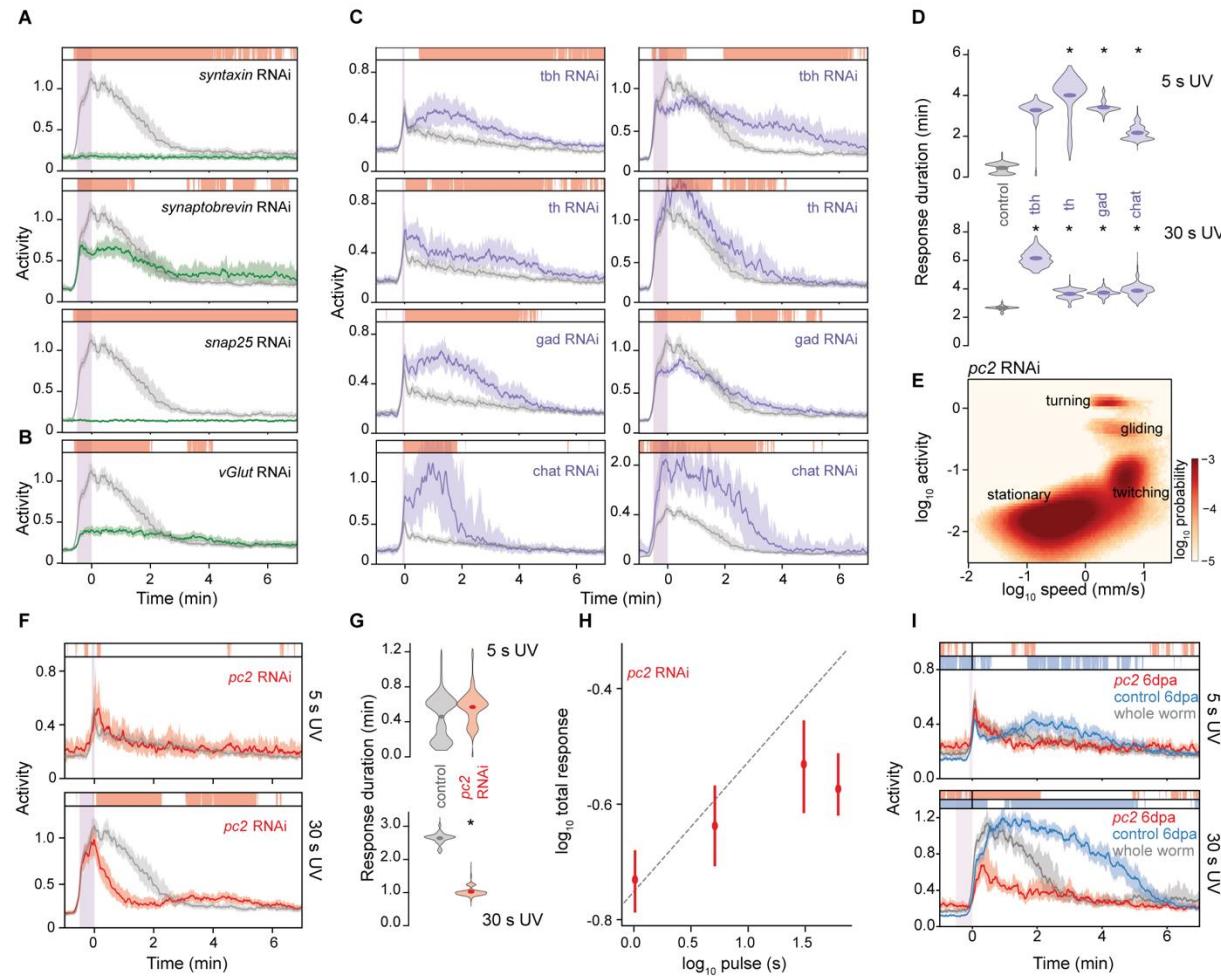
Figure 2: Peptide and small-molecule signals play opposing roles in regulating UV responses.

(A) Responses to UV stimulation after disrupting components of the SNARE core complex. Purple bar: duration of UV stimulation.

(B) Responses to UV stimulation after *vglut* RNAi.

(C) Responses to UV stimulation after disrupting small-molecule neurotransmitter syntheses.

(D) Duration of post-stimulus activity under RNAi and control conditions. Symbols: mean estimate from 1,000 non-parametric bootstrap samples; histograms: bootstrapped sampling distribution.

(E) Joint distribution of activity and speed after *pc2* RNAi under continuous UV simulation.

832 **(F)** Left: UV response after *pc2* RNAi. Right: Duration of post-stimulus activity is reduced after

833 *pc2* RNAi.

834 **(G)** Duration of post-stimulus activity under *pc2* RNAi and control conditions. Symbols: mean

835 estimate from 1,000 non-parametric bootstrap samples; histograms: bootstrapped sampling

836 distribution.

837 **(H)** Total response to UV stimulation of *pc2* RNAi animals saturates at high UV dose. Error bars:

838 99% CI. Line: anticipated power-law relationship (Extended Data Figure 2b).

839 **(I)** UV response in 6 dpa regenerating tails with (red) and without (blue) *pc2* RNAi. Gray: whole-

840 animal response.

841 Statistics. In (A), (B), (C), and (F), gray traces: RNAi controls; colored traces: RNAi of specific

842 genes. Bars above the traces in (A-D), (F), and (I) indicate times when the response is significantly

843 different from controls as measured by 1,000 nonparametric bootstrap comparisons of the two

844 populations ($p < 0.01$). Asterisks in (B) and (D) indicate $p < 0.01$, determined by 1,000 non-

845 parametric bootstrap comparisons of the difference in response duration between control and

846 RNAi groups.
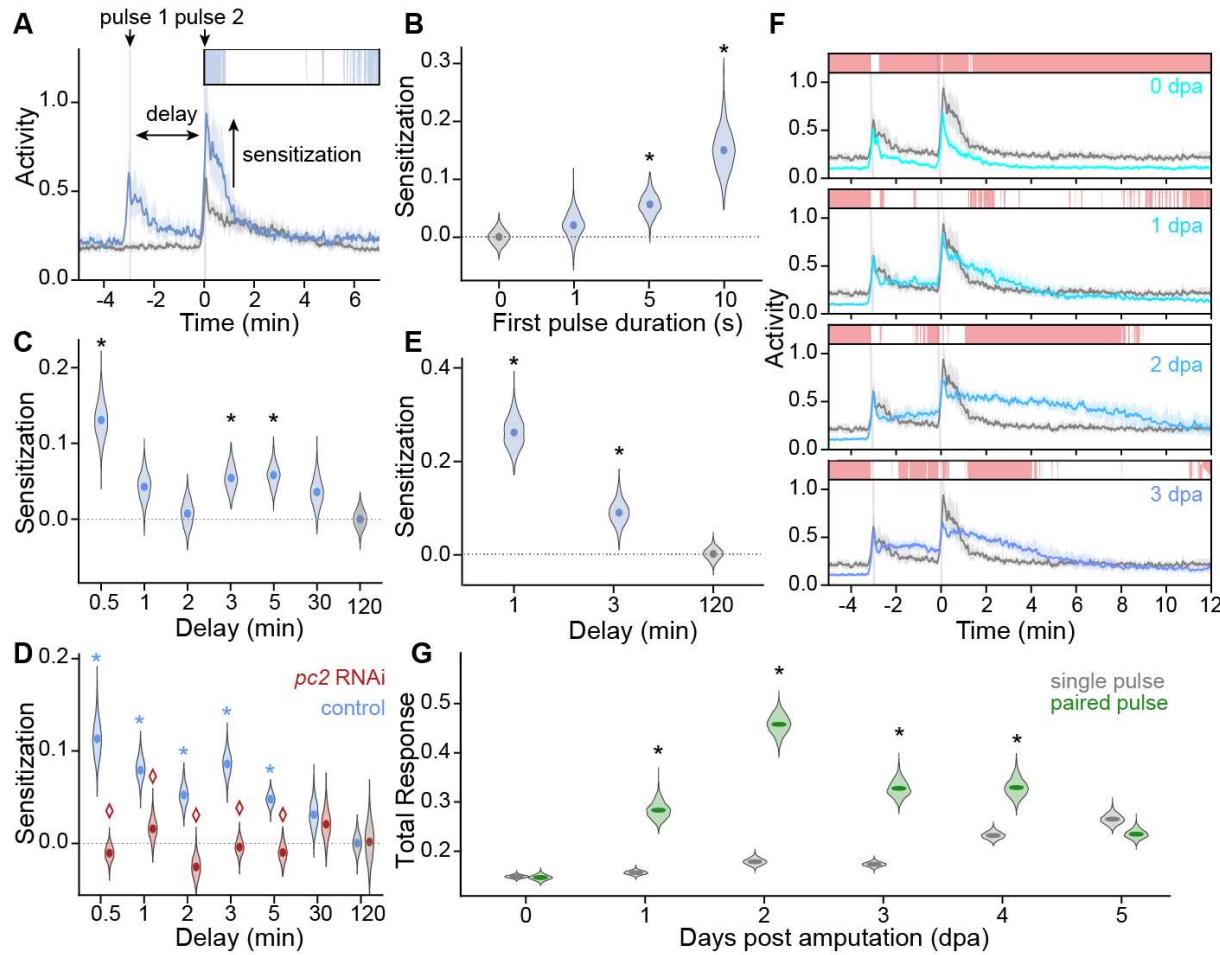
Figure 3: Neuropeptides are required for establishing short-term memory.

(A) Planarians show sensitization from prior UV exposure. Gray: response to single 5 s UV pulse; blue: response to paired 5 s pulses separated by 3 min delay. For all time traces, lines: median activity; shaded region: 99% CI.

(B) Sensitization, defined as the difference between total post-stimulus response to the second pulse and that of a single UV pulse after a 3 min delay, increases with the duration of the first UV pulse.

(C) Sensitization from two 5 s UV pulses vs. delay time.

(D) Sensitization is lost in *pc2* RNAi (red) animals.

(E) Mechanical vibration (5 s) sensitizes response to 5 s UV pulse.

858   **(F)** Response of paired 5 s UV pulses with 3 min delay through regeneration. Gray traces: whole-

859   animal controls; colored traces: regenerating tail fragments. Purple bar: duration of UV

860   stimulation.

861   **(G)** Total response in tail fragments to a single 5 s UV pulse (gray) and a 5 s pulse sensitized by

862   another 3 min prior (green) shows that the sensitization amplifies at early time points of

863   regeneration.

864   Statistics. Bars above the traces in (A) and (F): timepoints where activity in paired pulse is

865   significantly different from that of single pulse as measured by 1,000 nonparametric bootstrap

866   comparisons ($p < 0.01$). For all violin plots, symbols: mean estimate of sensitization using 1,000

867   non-parametric bootstrap samples of both the paired and single pulse conditions; histograms:

868   bootstrapped sampling distribution. Asterisks: sensitization significantly greater than zero ($p <$

869   0.01); diamond: significant difference in sensitization between control and *pc2* RNAi ($p < 0.01$).
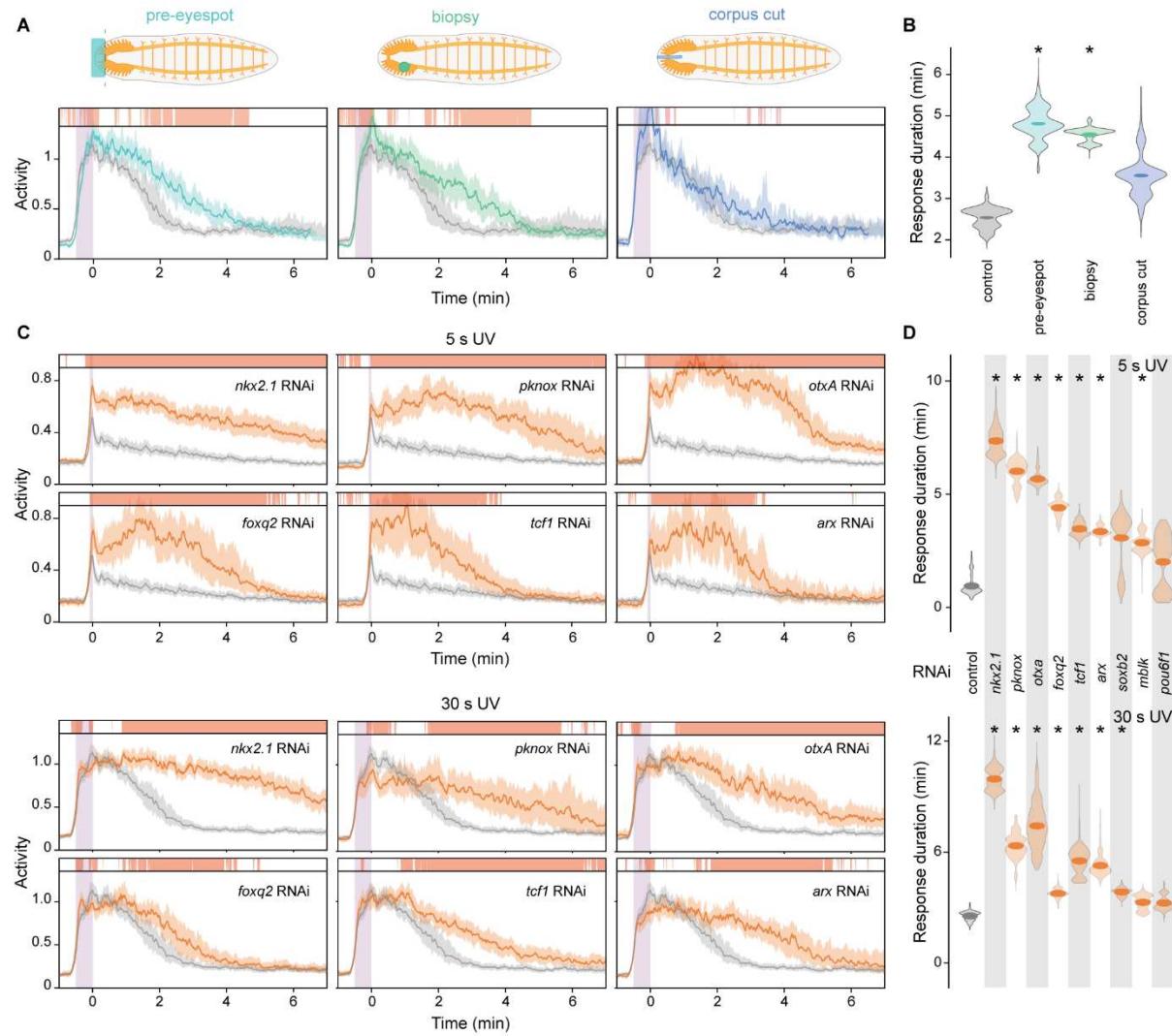
Figure 4: Excess activity is a signature of perturbed neural structure.

(A) Response to 30 s UV shows extended activity after various minor injuries. Colored traces: injured animals at 1 dpa; gray traces: whole-animal controls. Purple bar: duration of UV stimulation.

(B) Violin plot showing the duration of post-stimulus activity. Symbols: mean estimate from 1,000 non-parametric bootstrap samples; histograms: bootstrapped sampling distribution. Asterisks: p < 0.01 comparing injured and whole-animal responses.

(C) Response to 5 s (top) and 30 s (bottom) UV after knockdown of neural TFs. Orange traces:

879   RNAi; gray traces: control.

880   **(D)** Response duration after RNAi. Asterisks: p < 0.01 comparing RNAi and control conditions.

881   Statistics. Bars above the traces in (a) and (c) indicate the time when the response is significantly

882   different from whole-animal controls as measured by 1,000 nonparametric bootstrap comparisons

883   of the two populations (p < 0.01). Solid lines: median activity; shaded region: 99% CI; p-values in

884   (B) and (D) are determined by 1,000 non-parametric bootstrap comparisons of the difference in

885   response duration between the two groups.

886
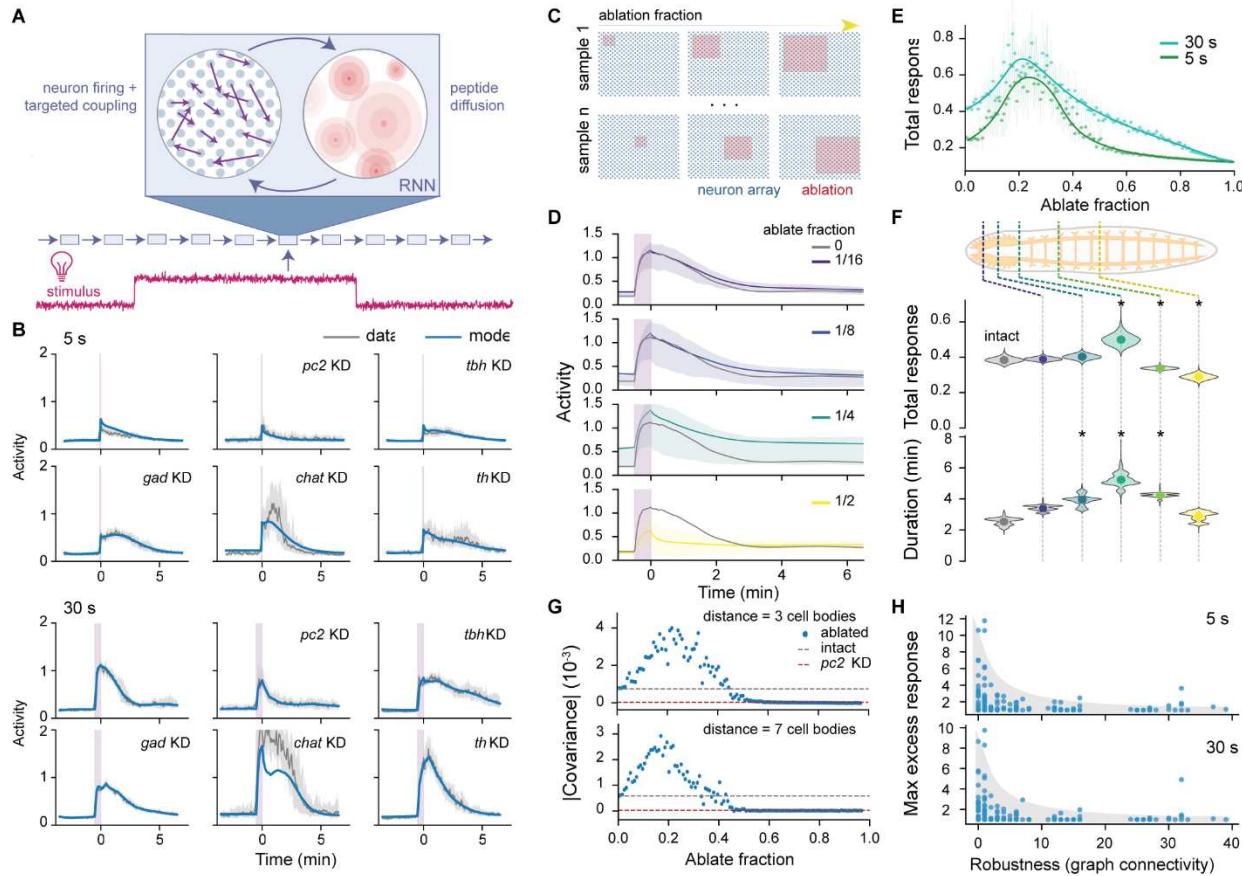
Figure 5: A RNN model recapitulates functional robustness after neural injury.

(A) Schematic of the dual-channel RNN model showing the feedback between peptidergic and small-molecule signaling.

(B) Output of model trained to emulate planarian responses under various stimulation and knockdown (KD) conditions. Gray: experimentally measured median activity; shaded region: 99% CI; blue: model response.

(C) Schematic of neural ablation within the model. Red regions are spatially contiguous populations of neurons with firing rates fixed at zero. For each ablation fraction, 200 regions are randomly sampled.

(D) Model response to 30 s UV stimulation at different ablation fractions. Gray: response of intact model; colored: mean activity over 200 sampled ablations; shaded region: interquartile value of

898   activities across ablation samples.

899   **(E)** Total response after ablations shows excess activity at moderate ablation fractions. Symbols:

900   average total response across ablations; error bars: 99% CI from 1,000 non-parametric bootstrap

901   samples; solid lines: polynomial interpolation.

902   **(F)** Planarian response to 30 s UV shows similar trends with increasing ablation as in the model.

903   Landmarks for amputation (top): anterior-end of eyespot, posterior end of eyespot, one eyespot

904   length posterior to eyespot, midway between eyespot and pharynx, mid-pharynx. Data for all

905   injured conditions are collected at 1 dpa. Symbols: mean estimate from 1,000 non-parametric

906   bootstrap samples; histograms: bootstrapped sampling distribution. Asterisks: $p < 0.01$ comparing

907   amputated and intact worms.

908   **(G)** Magnitude of spatial covariance of firing rates, which provides a quantification of the relative

909   contributions of the two communication mechanisms. Expectedly, the spatial covariance was lost

910   with *pc2* knockdown, but amplified when reducing small-molecule signals (Extended Data Figure

911   6b). Distances at which the covariance is measured correspond to the diffusion length scales of the

912   two peptides in the trained RNN model.

913   **(H)** Ablation-induced excess activity diminishes with increasing connectivity network robustness

914   quantified by the graph connectivity. Each dot represents an independently trained RNN with

915   different connectivity networks. The maximum excess response is defined as the ratio of maximum

916   average total response at any ablation level and the total response in the intact model.
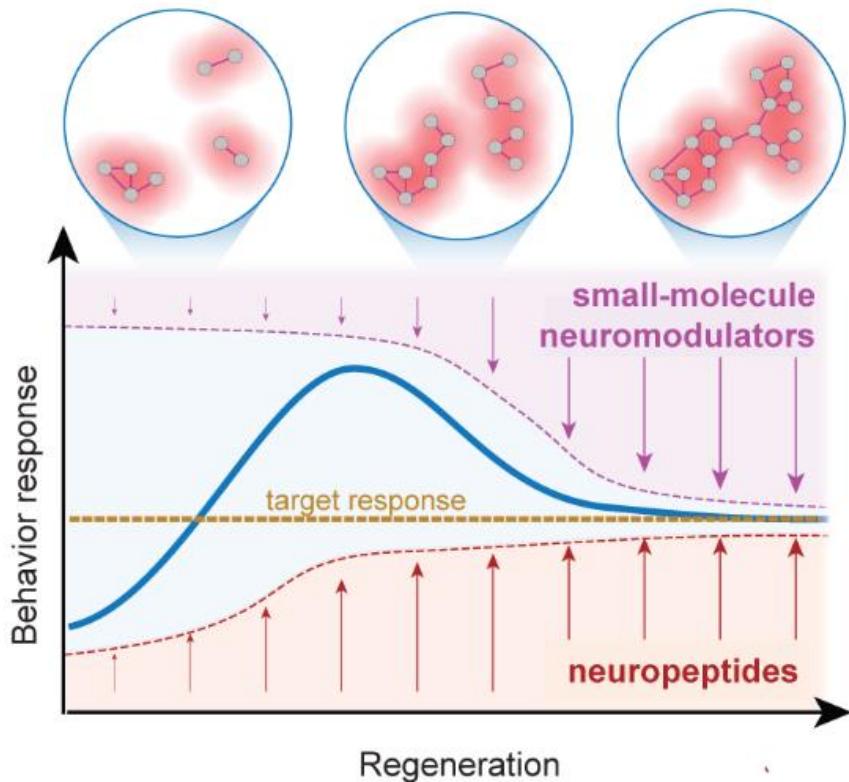
918 **Figure 6: Adaptive robustness through multi-channel signaling.**

919 Long range peptide signals (red) and targeted small-molecule signaling (purple) form a dual-

920 channel network and competitively regulate behavioral output (bottom). Under highly disrupted

921 post-amputation conditions (top left), the functions of both systems are compromised. As

922 regeneration proceeds, peptides can rapidly establish communication via long-range volumetric

923 diffusion to drive behavioral output, while the fragile targeted network remains fragmented

924 dysfunctional (top middle). The transient dominance of peptidergic signals at this stage leads to

925 excess activity in response to stimuli, which is then gradually refined as the connectome and

926 targeted small-molecule signaling re-establishes. When regeneration is complete, both

927 transmission mechanisms are restored and the behavior is constrained to the proper response (top

928 right).

Supplemental Figures
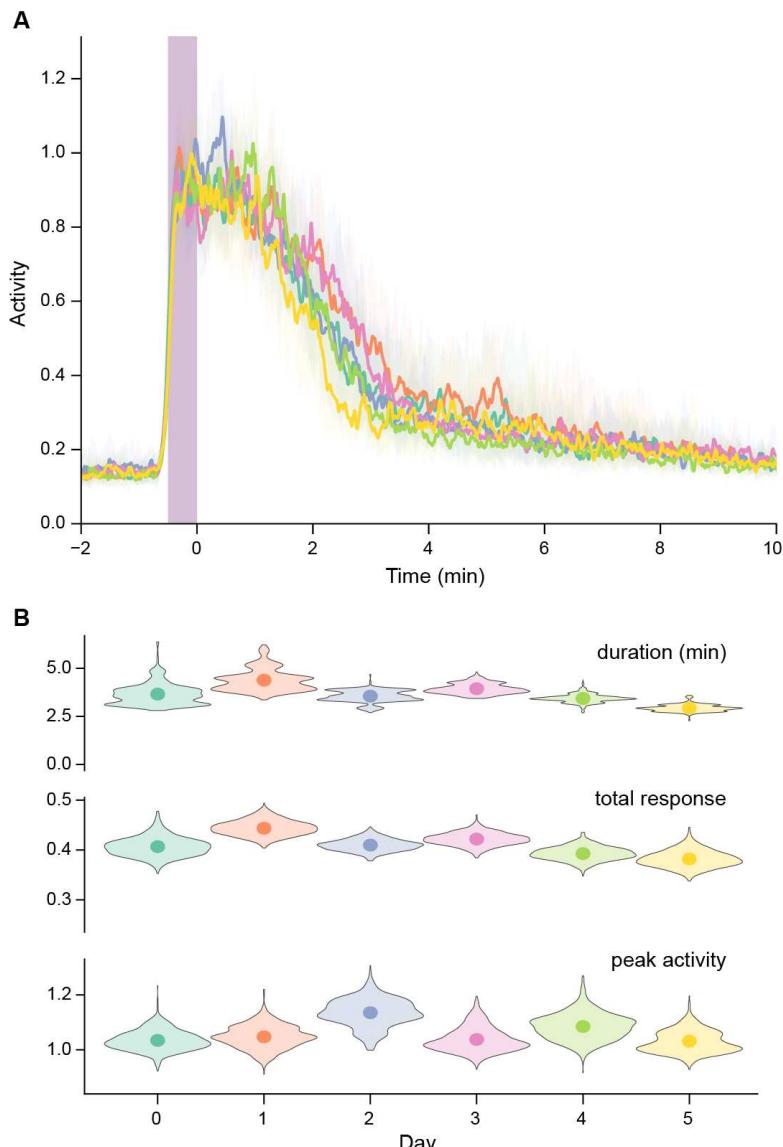
Figure S1: Planarians exhibit consistent behaviors throughout continuous imaging. Related to Figure 1

(**A**) Activity response of whole animals exposed to 30 s UV pulses every 2 hr across days in the imaging chamber. Purple bar: period of UV stimulation. Lines: median activity; shaded region: 99% CI as estimated by 1,000 non-parametric bootstrap samples.

50

937   **(B)** Quantification of responses shows no change across days. Symbols: mean estimate of

938   measurement on each day; histogram: sampling distribution from 1,000 non-parametric bootstrap

939   samples. No significant differences in the response measurements were found across days relative

940   to the first day in the chamber as determined by 1,000 paired bootstrap samples from each

941   condition ($p < 0.01$).
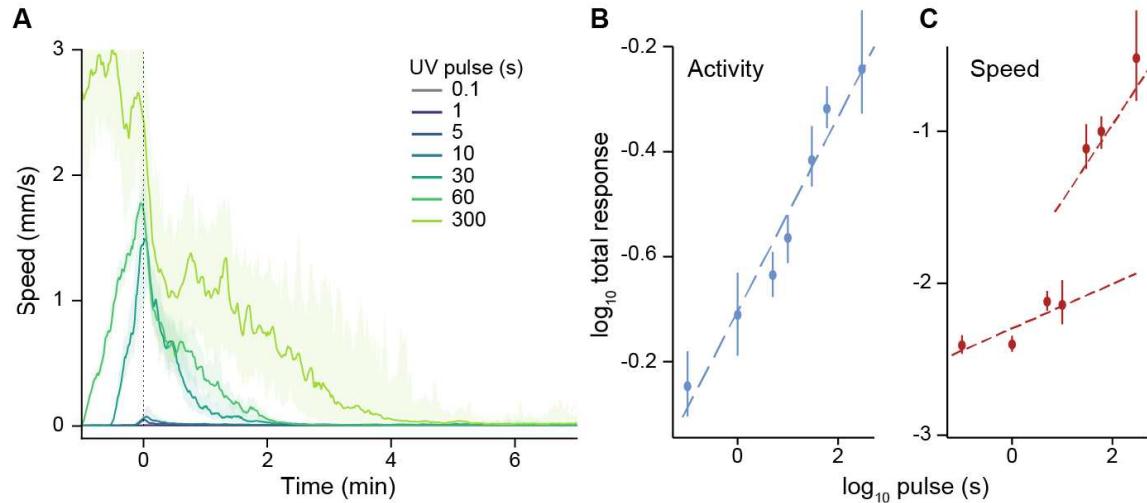
Figure S2: Activity scales as power law with total stimulation. Related to Figure 1

(A) Response of whole animals to UV as measured by speed. Time zero: end of UV stimulation.

Solid lines: median speed; shaded region 99% CI as estimated by 1000 non-parametric bootstrap samples.

(B) Total post-stimulus activity follows a power-law scaling with the duration of UV stimulus (slope = 0.18). Error bars: 99% CI.

(C) Total post-stimulus speed response scales with duration of the UV pulse only in the high-stimulus regime. Error bars: 99% CI.

951
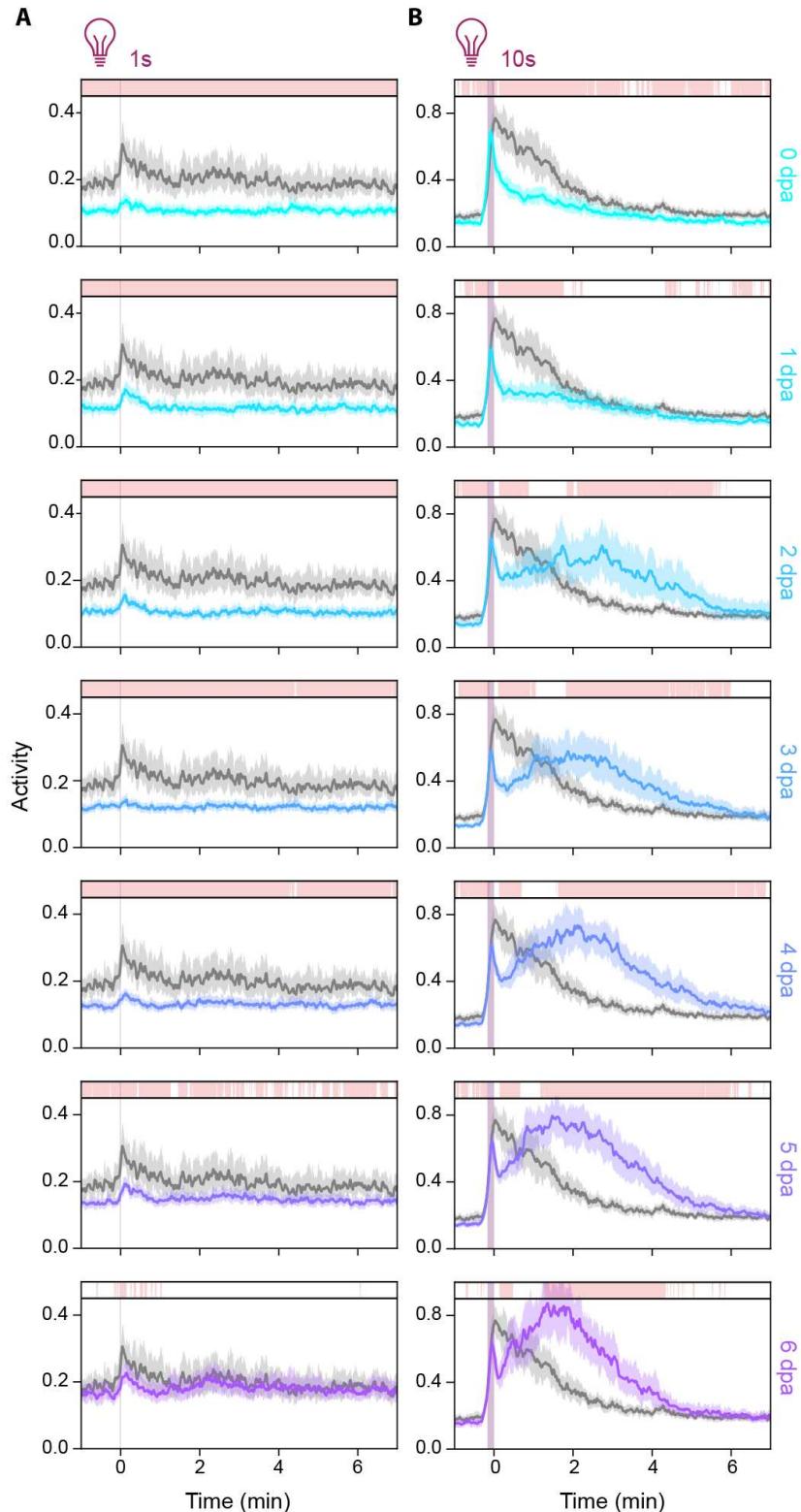
Figure S3: Response to additional UV stimuli after head amputation. Related to Figure 1

953   Response to 1 s (left) and 10 s (right) UV pulses, by tail fragments after amputation. Gray: whole-

954   animal controls; colored: regenerating tail fragments on each day post amputation (dpa). Bars

955   above the traces indicate time when the response of regenerating animals is significantly different

956   from whole-animal controls as measured by 1,000 nonparametric bootstrap comparisons of the

957   two populations (p < 0.01). Solid lines: median activity; shaded region: 99% CI.
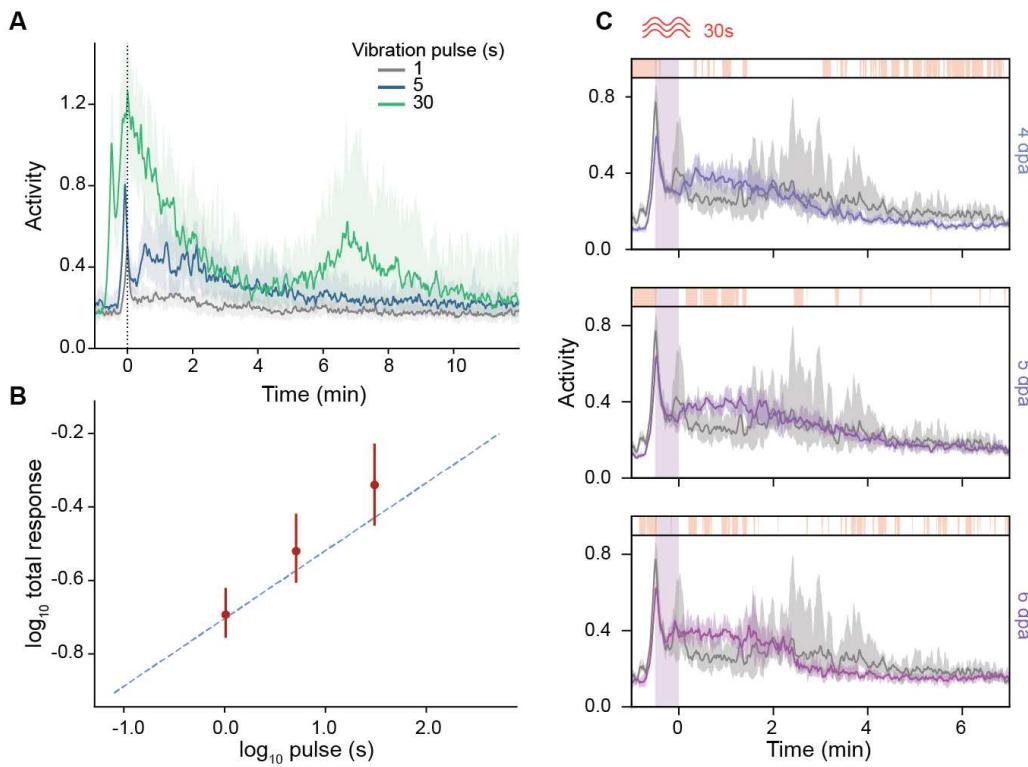
Figure S4: Response to vibration follows similar trends as those to UV. Related to Figure 1

(A) Response of whole animals to vibrational pulses. Time zero: end of stimulation. Solid lines: median speed; shaded region 99% CI as estimated by 1,000 non-parametric bootstrap samples.

(B) Total activity scale with the duration of the vibrational stimulation. Error bars: 99% CI. Dashed line: a power-law scaling with a slope of 0.18 as seen with UV stimulation.

(C) Response to 30 s vibration in regenerating tail fragments after amputation. Gray: whole-animal response; colored: regenerating response on a given day post amputation (dpa). Bars above the traces indicate time when the response of regenerating animals is significantly different from whole-animal controls as measured by 1,000 nonparametric bootstrap comparisons of the two populations ($p < 0.01$). For all time traces, lines: median activity; shaded region 99% CI. All confidence intervals are determined from 1000 non-parametric bootstrap samples.

970
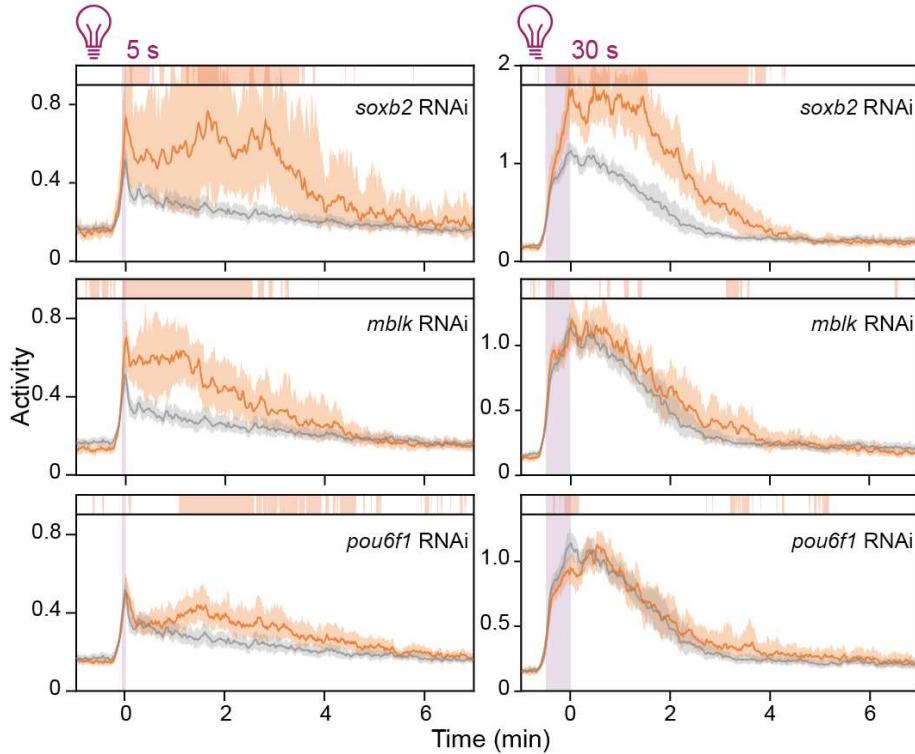
Figure S5: Additional behavioral phenotypes after TF knockdown. Related to Figure 4

Whole-animal response to 5 s (left) and 30 s (right) UV pulses after knockdown of neural TFs.
Orange: RNAi conditions; gray: control animals. Bars above the traces indicate time when the
response of regenerating animals is significantly different from whole-animal controls as measured
by 1,000 nonparametric bootstrap comparisons of the two populations ($p < 0.01$). Solid lines:
median activity; shaded region: 99% CI.

977
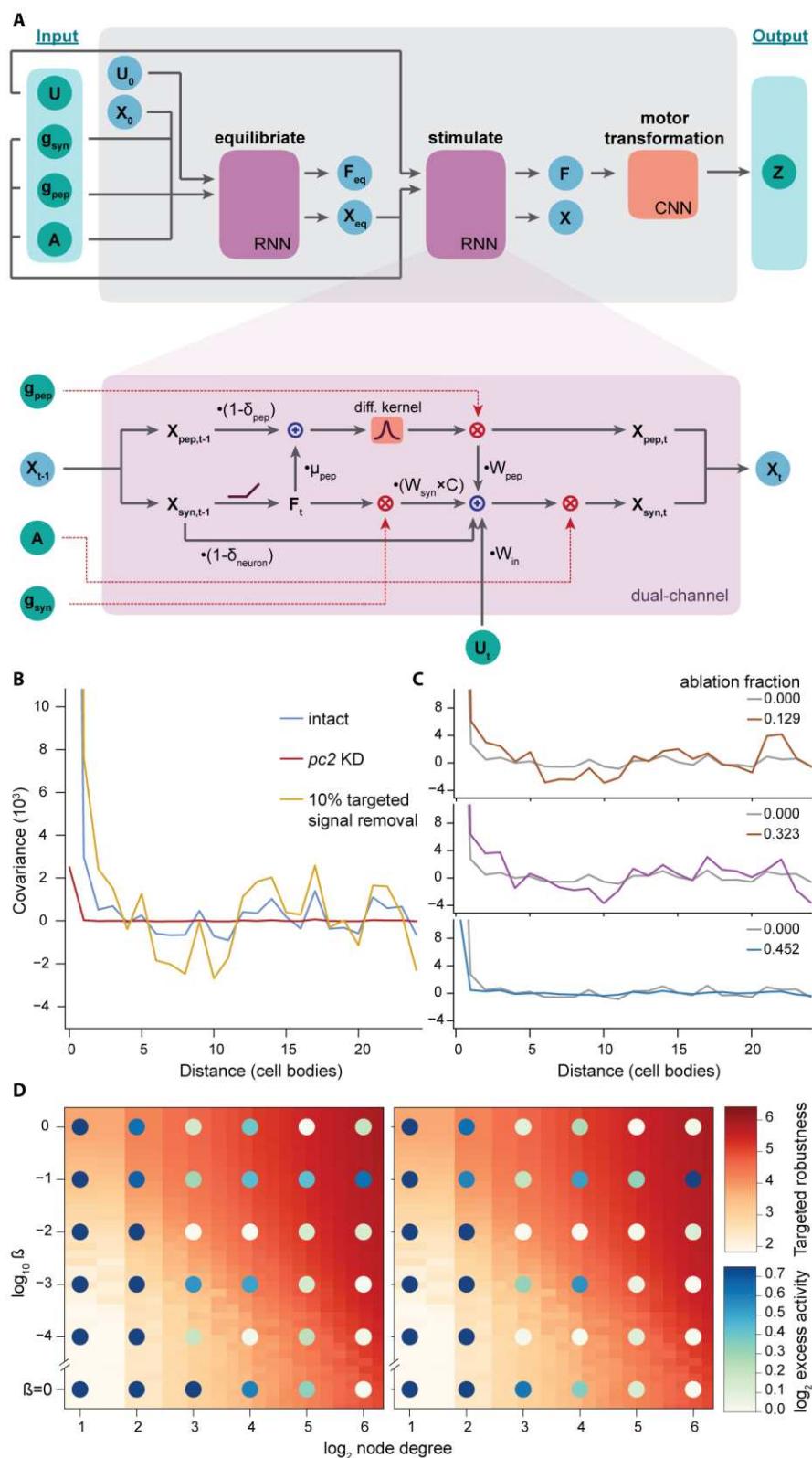
Figure S6: A modified RNN model to take into account the function of neuropeptides.

Related to Figure 5

(A) Diagram of the dual-channel neuron model. Top: Complete architecture of the model. Bottom: Operations performed at each timestep within the dual-channel RNN cell.

(B) Spatial covariance of firing rates is driven by peptidergic signals but interfered by small-molecule signals. The initial peak and trough in covariance within the intact model roughly correspond to the diffusive length scale of the excitatory (~3 cell bodies) and inhibitory (~7 cell bodies) peptides, respectively. Removing targeted links increases covariance (gold). Conversely, removing neuropeptides eliminates all spatial covariance (red).

(C) The magnitude of spatial covariance increases and then decays with increasing ablation.

(D) Ablation-induced excess activity is dependent on the robustness of connectivity network. Excess activity is defined as the maximum average total response at any ablation level normalized by the total response in the unabated model. Robustness of the connectivity network is estimated using inverse average edge centrality.

992 **Supplemental files**

993

994 **Supplemental Movie 1: Activity score captures broad range of animal movements. Related**

995 **to Figure 1**

996 The movie records the response of a planarian to a 5 s UV pulse within a droplet. Activity (cyan)

997 resolves non-traversal movements such as nodding and turning better than speed (gray). Shaded

998 region (purple) indicates period of UV stimulation.

999

1000 **Supplemental Movie 2: *vglut* knockdown causes uncoordinated motor activity. Related to**

1001 **Figure 2**

1002 The movie records the spontaneous behavior of a planarian after *vglut* RNAi. Animals fail to

1003 achieve translational movements and display eccentricities of muscular activities.

1004

1005 **Supplemental Movie 3: *pc2* knockdown animals show range of behavior. Related to Figure**

1006 **2**

1007 Examples of crawling and turning movements in *pc2* RNAi planarians under 30 min continuous

1008 UV stimulation. Each clip is from a different animal within the experiment.

1009

1010 **Supplemental Table 1: Primers used in this study. Related to STAR Methods**

1011 Listed are conventional name, contig number, and forward and reverse primers used in cloning

1012 experiments for RNAi knockdown.

1013

1014 **Supplemental Table 2: Trial replicate reporting. Related to Figure 1-4**

1015   Number of pulse trials for each experimental condition.